

AFIT/GE/ENG/04-18



CROSS RANGE SMEAR CHARACTERIZATION IN XPATCH ISAR IMAGES

THESIS

Peter E Muend
Captain, USAF

AFIT/GE/ENG/04-18

DEPARTMENT OF THE AIR FORCE

AIR UNIVERSITY

AIR FORCE INSTITUTE OF TECHNOLOGY

Wright-Patterson Air Force Base, Ohio

APPROVED FOR PUBLIC RELEASE; DISTRIBUTION UNLIMITED

The views expressed in this thesis are those of the author and do not reflect the official policy or position of the United States Air Force, Department of Defense, or the United States Government.

AFIT/GE/ENG/04-18

CROSS RANGE SMEAR CHARACTERIZATION IN XPATCH
ISAR IMAGES

THESIS

Presented to the Faculty
Department of Electrical and Computer Engineering
Graduate School of Engineering and Management
Air Force Institute of Technology
Air University
Air Education and Training Command
In Partial Fulfillment of the Requirements for the
Degree of Master of Science in Electrical Engineering

Peter E Muend, B.S.E.E.
Captain, USAF

March, 2004

APPROVED FOR PUBLIC RELEASE; DISTRIBUTION UNLIMITED

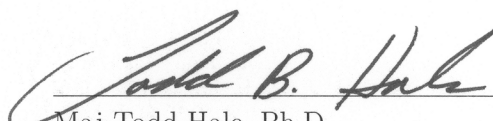
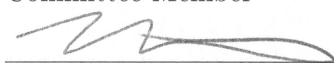
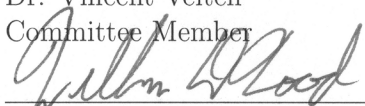
CROSS RANGE SMEAR CHARACTERIZATION IN XPATCH
ISAR IMAGES

THESIS

Peter E Muend, B.S.E.E.

Captain, USAF

Approved:

 Maj Todd Hale, Ph.D. Thesis Advisor	<u>18 FEB 04</u> Date
 Dr. Michael Temple Committee Member	<u>18 Feb 04</u> Date
 Dr. Vincent Velten Committee Member	<u>18 Feb 04</u> Date
 Maj William Wood, Ph.D. Committee Member	<u>18 Feb 04</u> Date

Acknowledgements

I would like to thank several organizations who all made this research possible.

The Air Force Research Laboratory (AFRL) Sensors Directorate Signature Modeling Branch, AFRL/SNAS, sponsored this work. Their personnel and contractors were invaluable while becoming knowledgeable in Xpatch[®]. In addition, they provided me all the CAD geometries I requested, saving me countless hours.

The Science Applications International Corporation (SAIC) Demaco Xpatch[®] team was extraordinarily helpful and always ready with explanations and suggestions.

This work was supported in part by a grant of computer time from the DoD High Performance Computing Modernization Program at the Army Research Lab (ARL) Major Shared Resource Center (MSRC) at Aberdeen Proving Grounds, Maryland. Without their computer resources, the large amount of processing required in this research would not have been possible. Every step of the way, their personnel were willing and eager to help out; I apologize for hogging almost half of their supercomputer.

Most importantly, however, I would like to thank my family and friends. They were all very understanding and supportive through this entire experience.

Peter E Muend

Table of Contents

	Page
Acknowledgements	iv
List of Figures	viii
List of Tables	x
List of Symbols	xi
List of Abbreviations	xii
Abstract	xiii
I. Introduction	1
1.1 Background	1
1.2 Problem	2
1.3 Previously Proposed Solution	4
1.4 Research Overview & Chapter Layout	5
1.5 Assumptions	6
II. Analytical Development	8
2.1 Introduction	8
2.2 Shooting And Bouncing Rays	8
2.2.1 Ray Density	9
2.2.2 First Bounce Algorithm	10
2.2.3 Maximum Bounces	11
2.2.4 Contributing Bounces	11
2.2.5 Higher Order Bounces	11
2.2.6 Divergence Factor	11
2.2.7 Diffraction	12
2.3 Inverse Synthetic Aperture Radar	12
2.3.1 Bandwidth	18
2.3.2 Frequency Center	20
2.3.3 Frequency Increment	21
2.3.4 Angular Span	21
2.3.5 Angular Increment	22
2.4 SBR and ISAR Interaction	22
2.4.1 Ray Density	23

	Page
2.4.2	Angular Increment 25
2.4.3	Angular Span 25
2.4.4	Frequency Center 25
2.4.5	Frequency Increment 26
2.4.6	Bandwidth 26
2.5	Smear Assessment Algorithm 27
2.5.1	Analysis of Maximum Smear 29
2.5.2	Analysis of Minimum Smear With Single Point Scatterer 30
2.5.3	Analysis of Minimum Smear With Multiple Point Scatterers 32
III.	Methodology 36
3.1	Introduction 36
3.2	Target Geometries 37
3.2.1	Flat Rectangular Plate 40
3.2.2	Ridged Plate 40
3.2.3	Slicy 42
3.3	Parameters 43
3.3.1	Variable Parameters 43
3.3.2	Constant Parameters 45
3.4	Cross Range Smear Characterization 48
3.5	Cross Range Smear Reduction 54
IV.	Cross Range Smear Characterization Results 55
4.1	Introduction 55
4.2	Flat Rectangular Plate 56
4.3	Ridged Plate 58
4.4	Slicy 61
4.5	Conclusions 63
V.	Cross Range Smear Reduction Results 66
5.1	Introduction 66
5.2	Flat Rectangular Plate 66
5.3	Ridged Plate 71
5.4	Slicy 78
5.5	Conclusions 88

	Page
VI. Conclusions	90
6.1 Introduction	90
6.2 General Discussion	90
6.3 Future Work	91
Bibliography	92

List of Figures

Figure		Page
1.1.	Example of No Cross Range Smear	3
1.2.	Example of No Cross Range Smear	3
2.1.	Shooting Grid	10
2.2.	Linear Projection	15
2.3.	Spatial Frequency Annulus	19
2.4.	ISAR Image Generation Flowchart	23
2.5.	Example of Maximum Smear	31
2.6.	Example of Minimum Smear with a Single Point Scatterer . .	33
2.7.	Example of Minimum Smear with Three Point Scatterers . .	35
2.8.	Example of Minimum Smear with Five Point Scatterers . . .	35
3.1.	ISAR Aperture Orientation	39
3.2.	Flat Plate Geometry	40
3.3.	Ridged Plate Geometry	41
3.4.	Slicy Geometry	42
5.1.	Flat Rectangular Plate Max Smear Reduction	67
5.2.	Flat Rectangular Plate Mean Smear Reduction	67
5.3.	Flat Rectangular Plate Run 16 3-Aspect Smear	68
5.4.	Flat Rectangular Plate Run 16 3-Aspect Difference	68
5.5.	Flat Rectangular Plate Run 16 9-Aspect Smear	69
5.6.	Flat Rectangular Plate Run 16 9-Aspect Difference	69
5.7.	Flat Rectangular Plate Run 16 Original Image	69
5.8.	Flat Rectangular Plate Run 16 3-Aspect Filtered Image . . .	70
5.9.	Flat Rectangular Plate Run 16 9-Aspect Filtered Image . . .	70
5.10.	Flat Rectangular Plate Run 5 3-Aspect Smear	71
5.11.	Flat Rectangular Plate Run 5 3-Aspect Difference	71
5.12.	Flat Rectangular Plate Run 5 9-Aspect Smear	72
5.13.	Flat Rectangular Plate Run 5 9-Aspect Difference	72
5.14.	Flat Rectangular Plate Run 5 Original Image	72
5.15.	Flat Rectangular Plate Run 5 3-Aspect Filtered Image	73
5.16.	Flat Rectangular Plate Run 5 9-Aspect Filtered Image	73
5.17.	Ridged Plate Max Smear Reduction	74
5.18.	Ridged Plate Mean Smear Reduction	75
5.19.	Ridged Plate Run 19 3-Aspect Smear	76
5.20.	Ridged Plate Run 19 3-Aspect Difference	76

Figure	Page
5.21. Ridged Plate Run 19 9-Aspect Smear	76
5.22. Ridged Plate Run 19 9-Aspect Difference	76
5.23. Ridged Plate Run 19 Original Image	77
5.24. Ridged Plate Run 19 3-Aspect Filtered Image	77
5.25. Ridged Plate Run 19 9-Aspect Filtered Image	78
5.26. Ridged Plate Run 8 3-Aspect Smear	79
5.27. Ridged Plate Run 8 3-Aspect Difference	79
5.28. Ridged Plate Run 8 9-Aspect Smear	79
5.29. Ridged Plate Run 8 9-Aspect Difference	79
5.30. Ridged Plate Run 8 Original Image	80
5.31. Ridged Plate Run 8 3-Aspect Filtered Image	80
5.32. Ridged Plate Run 8 9-Aspect Filtered Image	81
5.33. Slicy Max Smear Reduction	82
5.34. Slicy Mean Smear Reduction	82
5.35. Slicy Run 12 3-Aspect Smear	83
5.36. Slicy Run 12 3-Aspect Difference	83
5.37. Slicy Run 12 9-Aspect Smear	84
5.38. Slicy Run 12 9-Aspect Difference	84
5.39. Slicy Run 12 Original Image	84
5.40. Slicy Run 12 3-Aspect Filtered Image	85
5.41. Slicy Run 12 9-Aspect Filtered Image	85
5.42. Slicy Run 1 3-Aspect Smear	86
5.43. Slicy Run 1 3-Aspect Difference	86
5.44. Slicy Run 1 9-Aspect Smear	86
5.45. Slicy Run 1 9-Aspect Difference	86
5.46. Slicy Run 1 Original Image	87
5.47. Slicy Run 1 3-Aspect Filtered Image	87
5.48. Slicy Run 1 9-Aspect Filtered Image	88

List of Tables

Table		Page
3.1.	Geometries	38
3.2.	Variable Parameters	44
3.3.	Constant Parameters	46
3.4.	DOE Runs	53
4.1.	Flat Rectangular Plate Smear Data	57
4.2.	Flat Rectangular Plate Smear Model	58
4.3.	Ridged Plate Smear Data	59
4.4.	Ridged Plate Smear Model	60
4.5.	Slicy Smear Data	62
4.6.	Slicy Smear Model	63

List of Symbols

Symbol		Page
λ	Wavelength	9
G	Transform of Reflectivity Density	13
P_θ	Transform of Linear Projection of Reflectivity Density	13
θ	Incident Angle of Illumination	13
U	Spatial Frequency Domain	13
p_θ	Linear Projection of Reflectivity Density	13
u	Spatial Domain	13
ω_0	Pulse Center Frequency	14
α	Pulse Ramping Constant	14
Π	Rectangular Envelope Function	14
τ_c	Time length of signal	14
g	Reflectivity Density	14
A	Attenuation Constant	14
R	Distance to Reflectivity Density Center	14
c	Speed of Light in Free Space	14
δ_{range}	Range Resolution	18
B	Bandwidth	18
λ_0	Pulse Center Wavelength	21
δ_f	Frequency Increment	21
Δ_{range}	Range Extent	21
Δ_θ	Angular Span	22
$\delta_{\text{crossrange}}$	Cross Range Resolution	22
$\Delta_{\text{crossrange}}$	Cross Range Extent	22
δ_θ	Angular Increment	22
R^2	Percentage of System Explained by Model	52

List of Abbreviations

Abbreviation		Page
AFRL	Air Force Research Laboratory	iv
SAIC	Science Applications International Corporation	iv
DoD	Department of Defense	iv
ARL	Army Research Lab	iv
MSRC	Major Shared Resource Center	iv
CEM	Computational Electromagnetics	1
ISAR	Inverse Synthetic Aperture Radar	1
2-D	Two-Dimensional	1
SAR	Synthetic Aperture Radar	1
SAIC	Science Applications International Corporation	2
EM	Electromagnetic	4
SBR	Shooting and Bouncing Rays	4
SBR	Shooting and Bouncing Rays	8
EM	Electromagnetic	8
ISAR	Inverse Synthetic Aperture Radar	8
2-D	Two-Dimensional	8
GO	Geometrical Optics	8
PO	Physical Optics	8
IGES	Initial Graphics Exchange Specification	12
1-D	One-Dimensional	13
GHz	Gigahertz	18
Hz	Hertz	20
ISAR	Inverse Synthetic Aperture Radar	36
SBR	Shooting and Bouncing Rays	36
DOE	Design of Experiments	37
CAD	Computer Aided Design	37
EM	Electromagnetic	37
DOFs	Degrees of Freedom	49
DOF	Degree of Freedom	49
SSR	Sum of Squares due to Regression	52
SST	Total Sum of Squares	52
ISAR	Inverse Synthetic Aperture Radar	55
EM	Electromagnetic	55
DOE	Design of Experiments	55
dB	Decibel	66
ISAR	Inverse Synthetic Aperture Radar	90

Abstract

This thesis investigates a cross range smear phenomenon seen in far field, frequency domain Xpatch[®] calculations. The phenomenon is very subtle, manifesting itself in 2-D ISAR images as a low-level scatterer response smeared in the cross range direction. This cross range smear occurs only using complex target models with certain characteristics. It is also a mathematical construct, not occurring in physical SAR systems. Using a carefully constructed scattering target set, Xpatch[®]-generated ISAR images are used to characterize cross range smear in terms of its input parameters. The characterization is done as a DOE-based polynomial approximation to the observed smear levels. Frequency extent and bandwidth have the highest effect on cross range smear, consistently increasing smear with parameter value. Ray density is slightly less important, having primarily squared and second order influence. The choice of diffraction and first bounce algorithm has very little effect on cross range smear. In addition, the performance of a proposed smear reduction technique is analyzed against Xpatch[®]-generated ISAR images. The algorithm generally reduces smear, but the smear reduction magnitude is not a linear function of smear value.

CROSS RANGE SMEAR CHARACTERIZATION IN XPATCH ISAR IMAGES

I. Introduction

1.1 Background

There have been great advances in the field of stealth design due to the advent of Computational Electromagnetics (CEM). Incorporating electromagnetic stealth into modern weapon system design enables great gains in lethality and survivability. These stealth aircraft penetrate deep into highly defended areas unseen and deliver ordinance onto previously unreachable targets.

CEM tools are commonly used to simulate electromagnetic scattering from targets, a key step in designing stealth aircraft. This scattered field is defined as the reflections off a target from incident electromagnetic waves—mathematically stated as the total field in the presence of the target minus the field with no target present. The incident waves are characterized as from a radar, friendly or adversarial. By simulating the electromagnetic scattering from the target, radar signatures can be developed. These signatures are used to analyze the target for radar vulnerabilities to be exploited or protected against, i.e., the application of stealth design.

Inverse Synthetic Aperture Radar (ISAR) images are often used as a two-dimensional (2-D) target signature. ISAR processing provides a scattering center map within 2-D space: range and cross range. A variation of spotlight Synthetic Aperture Radar (SAR), ISAR processes multiple target aspects from target rotation against a stationary radar platform into a 2-D scattering strength image. The ISAR image allows radar vulnerability analysis and automatic target recognition and classification.

Xpatch[®] is a popular CEM tool used to simulate and visualize electromagnetic scattering from target models, developed and distributed by Science Applications International Corporation (SAIC) and sponsored by government organizations such as the Air Force Research Laboratory. Xpatch[®] can generate a variety of target signatures from this scattering data, such as ISAR images. Xpatch[®] is used in many US Government and industry applications [1].

1.2 Problem

In certain ISAR image classes generated with Xpatch[®], a low-level smear is apparent in the cross range direction. An example of this smearing is illustrated in Figs. 1.1 and 1.2. Figure 1.1 shows an ISAR target image when constrained to a low dynamic range, where only strong scattering contributions are shown. Figure 1.2 shows the same target image constrained to a high dynamic range, including weaker responses masked in the low dynamic range image. While more overall scatterer response is evident in the high dynamic range image, as expected, an additional smearing effect in the cross range (vertical) direction is evident. This cross range smear is the subject of research.

The smearing is very subtle, manifesting itself in the ISAR image as an elongated scatterer response. It occurs at a very low-level; the smearing can only be observed in the SAR images when viewed with a high dynamic range, showing responses many orders of magnitude less than the overall peak response in the image.

Increasingly sensitive systems require images with a high dynamic range. These systems can distinguish low level responses from background noise. Hence, low level simulation errors become increasingly important problems when accurately simulating and modeling potential targets. Cross range smear, an anomalous artifact in simulated data, therefore represents an obstacle to be overcome in order to support these newer systems.

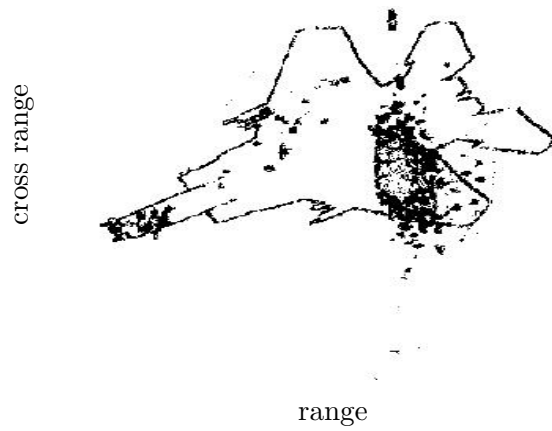


Figure 1.1: An ISAR image illustrating the 2-D scatterer response from a target, given a 30 dB dynamic range and incident ray density of 10 rays/ λ . No cross range smear is observed. *From [2].*

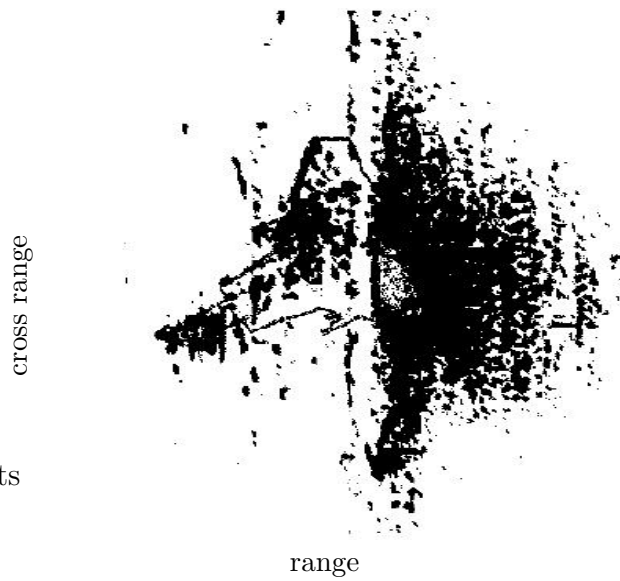


Figure 1.2: An ISAR image illustrating the 2-D scatterer response from a target, given a 55 dB dynamic range and incident ray density of 10 rays/ λ . Cross range smear is seen as elongated responses in the vertical direction. *From [2].*

Xpatch[®] uses two entirely different, user selectable, methods when forming ISAR images: frequency or time domain calculations. While the results *should* be substantially equivalent, cross range smearing is *only* evident in ISAR images formed through frequency domain calculations. ISAR images generated with time domain processing¹ do *not* show the same smearing effect.

Open literature documents the cross range smear present in Xpatch[®] ISAR images. Bhalla and Ling describe the effect in a 1997 IEEE article, where they attribute the smear to angular data scintillation noise [2]. However, a robust cross range smear characterization and complementary rationale for its presence is heretofore lacking. This research performs a characterization of cross range smear present in Xpatch[®] frequency domain ISAR images. This characterization is described in terms of target geometry, electromagnetic (EM) physics simulation technique, and ISAR image generation parameters.

1.3 Previously Proposed Solution

According to the Shooting and Bouncing Rays (SBR) technique used to calculate scattered field data (the precursor to ISAR images) in Xpatch[®], a dense grid of ray tubes is launched at the scattering target from each ISAR imaging position. Bhalla and Ling call the initial location and ray tube positioning the “shooting grid [2].” Each shooting grid position is located at a unique angle relative to the target, which translates to a unique spoke in the spatial frequency domain annulus². At each new position, no matter how small the position change, the grid moves to a corresponding angular location. This repositioning causes the grid-launched ray tubes to initially impact the target at different points during each ray shoot. The change in initial reflection locations is inevitable and happens regardless of shooting grid density or angular resolution. The target complexity coupled with the different

¹Xpatch[®] time domain processing is performed by calculated scattered field data from a single, central aspect and extrapolating the results over all other aspects in the SAR aperture.

²The concept of the spatial frequency domain annulus is described in Chapter III.

initial reflection points results in a vastly different scattered field, even for small angular changes in the shooting grid. Bhalla and Ling identified these sharp scattered field variations (a function of incident ray angle) as angular scintillation noise.

Bhalla and Ling propose two solutions to minimize the presence of cross range smear. The first, a spatial filtering algorithm, attenuates high-frequency scintillation noise. The second uses angular-extrapolation to fill in and smooth gaps between the discretely sampled SBR-calculated fields.

1.4 Research Overview & Chapter Layout

The purpose of this research is to characterize cross range smear in Xpatch[®] ISAR images. This characterization has two facets. First, cross range smear is characterized in terms of Xpatch[®] input parameters and target geometries. Second, a solution proposed by Bhalla and Ling, described in Sec. 1.3, is evaluated using a number of Xpatch[®]-generated ISAR images.

Chapter II presents an analytic development of key underlying concepts. The SBR technique, used by Xpatch[®] to calculate scattered fields, is described with its various input parameters. A mathematical development of ISAR follows, describing the concepts behind the transformation of scattered field data into a 2-D radar image. The last section of this chapter details the algorithm used to determine the amount of cross range smear contained in an ISAR image, necessary to perform the subsequent smear characterization and reduction evaluation.

Chapter III follows the analytical development with a methodology description. The geometries and parameter values used to generate Xpatch[®] ISAR images are described. The techniques used to characterize smear in terms its parameters are also detailed, as are the smear reduction application and subsequent performance analysis.

The results of both research facets, smear characterization and smear reduction analysis, are split into two chapters. Chapter IV presents the results of smear

characterization in terms of each target geometry, as well as a general discussion of the aggregate results. Chapter V presents the performance of the smear reduction technique, again in terms of individual geometries (but multiple ISAR images, given varying input parameters) and as an aggregate discussion.

Finally, Chapter VI presents final conclusions. A very general discussion of the results is given, along with direction for further related research.

1.5 Assumptions

Cross range smear is a concern due to the assumption that it is a *simulation* artifact, a result of the scattering algorithm. This assumption implies cross range smearing would *not* occur in ISAR images generated from measured data given an appropriately low noise floor.

This primary assumption also forms the basis for this research. If smearing were a physical effect present in ISAR images of measured data, Xpatch[®] would correctly model the important scattering physics involved. The scattered data would be correctly simulated (at least in terms of the phenomenon that produces the cross range smear) and there would be no need to characterize the smearing as a mathematical anomaly. Two primary reasons justify the assumption of cross range smear existing as only a simulation artifact.

First, cross range smear generated in Xpatch[®] utilizing time domain calculations does *not* exist. Since the time domain scattering and ISAR processing implementation differs significantly from the frequency domain implementation and cross range smear does not exist in images generated using the time domain processing, one (or both) of the processing methods is incorrect.

Second, ISAR images generated from measured data do *not* exhibit cross range smear. Since no simulation is involved when the scattered fields are directly measured, simulation-specific problems are removed as an error source. Assuming noise, present in all measured signals, does not mask cross range smear in measurement-

based ISAR images, the assumption that cross range smears in Xpatch[®] ISAR images are a simulation artifact is justified.

II. Analytical Development

2.1 Introduction

This chapter presents a description of the techniques used both by the Xpatch[®] program and the tools used to analyze its output for cross range smear. The Shooting and Bouncing Rays (SBR) technique, used by Xpatch[®] to calculate the scattered fields from a target illuminated by incident electromagnetic (EM) energy, is the first covered. The data calculated via SBR is then used as inputs into Inverse Synthetic Aperture Radar (ISAR) processing, described next. The ISAR processing generates a two-dimensional (2-D) image of the target initially radiated by the SBR technique; cross range smear, the subject of analysis, is sometimes visible within these ISAR images. Interactions between the SBR technique and ISAR processing are discussed after both are presented individually. Finally, a development of the algorithm used to analyze ISAR images for smear is presented. This algorithm is used to help assess which input factors influence the amount of smear present in an ISAR image.

2.2 Shooting And Bouncing Rays

SBR is the scattering simulation method used in Xpatch[®], the program that generates ISAR images that can display cross range smear. The SBR technique is used to generate the expected scattered return from a given illumination, such as by a simulated radar. SBR is derived from the combination of two well known high-frequency computational techniques: Geometrical Optics (GO) and Physical Optics (PO).

Balduaf et al described the SBR technique in 1991 when they presented a paper comparing SBR to measured data for several standard scattering targets [3]. SBR compared favorably to the measured data, especially with multiple-bounce targets at high frequencies.

In SBR, a densely packed grid of GO-type ray tubes is launched towards a CAD-generated target to calculate the scattered field when illuminated from that point. Each ray tube behaves according to the rules of GO until its last reflection. Physical target geometries that affect ray divergence, convergence, and polarization are all taken into account. At each ray tube reflection point, a PO surface current is calculated. The computed surface currents are then used (by reradiating those currents) to find the resulting scattered field.

For the case of cavity analysis, a slightly different approach is used [4]. Each ray tube that enters the cavity is reflected as before. However, the last reflection point is defined as the cavity opening. Aperture integration is used to calculate the “cavity equivalent” of surface currents. The scattered field due to these equivalent currents is then calculated.

Each ray tube individually contributes to a unique surface or equivalent current. Therefore, the entire scattered field must be updated for each ray tube launched at the target.

In the following sections, Xpatch[®] parameters are individually discussed.

2.2.1 Ray Density. As mentioned in Sec. 2.2, the individual GO ray tubes propagated towards the target are packed together into a densely packed grid. This grid, referred to as the shooting grid, is positioned at each incident radiation direction. The shooting grid defines the initial position of ray tubes to be propagated towards the target at each shooting grid position. The grid span is large enough to cover the entire projected target area, considering the target orientation and illumination direction. The ray tube density within the shooting grid is called the grid density. The higher the grid density, in rays per wavelength (λ), the more ray tubes are propagated towards the target from each position. Each ray tube is spaced regularly over the shooting grid. An example shooting grid layout is shown in Fig. 2.1.

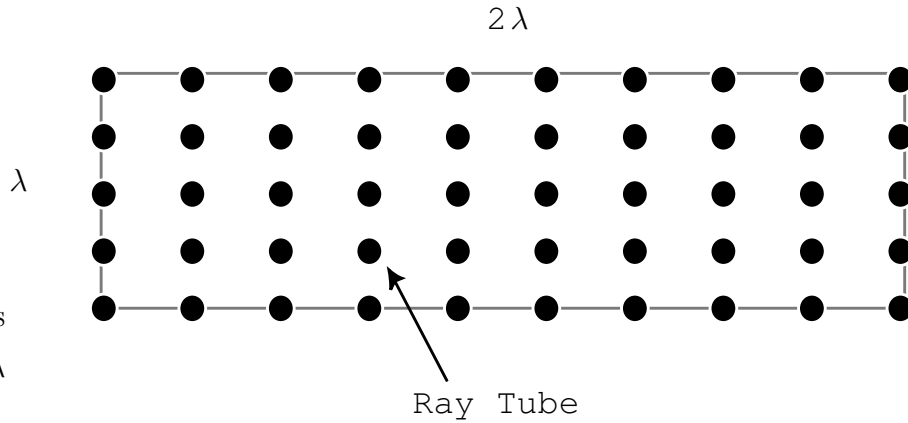


Figure 2.1: An illustration of the shooting grid from which ray tubes propagate towards a target in SBR scattering calculations. The shooting grid defines the initial position of the ray tubes, and in this case has a length of 2λ , height of λ , and grid density of 5 rays per λ .

2.2.2 First Bounce Algorithm. The first bounce algorithm parameter modifies the default behavior of Xpatch[®]'s use of the SBR technique when calculating scattered fields. The Xpatch[®] first bounce parameter has three options: SBR, PO, and Z-Buffer. The first two options, SBR and PO, are discussed. The Z-buffer option is not considered as it provides, according to the Xpatch[®] documentation, the least accurate result.

When SBR is used as the first bounce algorithm, incident rays are launched at the target from the direction of incidence. This behavior is consistent with the behavior of SBR at subsequent points of reflection. If target model surfaces are illuminated by a ray tube, a reflection is generated at that surface. However, if PO is used as the first bounce algorithm, each target model facet or patch is split into subsections. Visibility from these subsections to rays from the direction of incidence is determined and PO currents are calculated. PO provides a more accurate first bounce surface current model than SBR with an accompanying increase in computational time.

2.2.3 Maximum Bounces. The maximum bounces parameter is used in the Xpatch[®] SBR implementation to determine the number of reflections that each ray tube is allowed before truncation. This parameter is applicable to ray tubes that are reflected many times before reradiating off the target into free space. Limiting the number of reflections can decrease computation time at the cost of scattered field accuracy.

2.2.4 Contributing Bounces. Xpatch[®]'s SBR implementation allows for selection of which bounces contribute to the resulting scattered field. If the option for all bounces to contribute to the scattered field is selected, every reflection off a surface generates a surface current and, therefore, a scattered field. These fields are then added into the total scattered field result. This option is the most accurate. Alternatively, only the first and last bounces can be set to contribute to the total scattered field. This option reduces computation time, at the expense of accuracy.

2.2.5 Higher Order Bounces. Xpatch[®] can selectively choose which fields contribute to the surface currents at each SBR bounce point on the illuminated target. The surface currents are then used to calculate the resulting total scattered field. This parameter is applicable when all SBR reflections are set to contribute to the total scattered field, as in Sec. 2.2.4. Either both the scattered and incident field or only the incident field at each bounce point can be selected to contribute. When both the incident and scattered field contribute, both fields are used to determine the surface currents at each bounce point. If only the scattered field is selected, only the scattered field is used to determine the surface currents. The selection of both incident plus scattered fields produces the most accurate result.

2.2.6 Divergence Factor. Xpatch[®] can use the divergence factor, a function of surface curvature, to allow for ray tube spreading from bounces on curved surfaces. SBR ray divergence affects the cross sectional area of each ray tube, and therefore

the resulting scattered field from each bounce. This behavior is identical to how GO ray divergence is handled. This parameter does not apply to facetized target models since surface curvature is not defined. However, for target models defined in formats such as the Initial Graphics Exchange Specification (IGES), ray divergence is a factor.

2.2.7 Diffraction. Xpatch[®] can use a diffraction edge file to separately calculate scattered EM fields due to specified diffractive edges. Edge diffraction is calculated using Mitzner's incremental edge diffraction coefficient method, and is included only when this option is specified and the edge is unobstructed. The diffractive scattered field is coherently added to the scattered field calculated using SBR.

2.3 Inverse Synthetic Aperture Radar

ISAR, or inverse SAR, is the process used by Xpatch[®] to generate 2-D radar images of a given scattering target. By using data calculated by the SBR technique in Sec. 2.2, Xpatch[®] uses ISAR processing to generate a 2-D radar image of the target scene. These images can display the smearing phenomena that is the subject of research.

ISAR is a variation of spotlight mode SAR, a well established and very effective technique that provides high-resolution imagery of a spatial area by leveraging radar return information from multiple target aspects. Beamsteering is typically used to continually focus radar energy on a single target area, thereby generating the multiple aspect information. ISAR, as simulated in Xpatch[®], reverses the spotlight mode scenario by rotating the target while using a stationary radar. Target rotation generates the multiple aspects required by ISAR processing.

Munson established the basis for current spotlight mode processing techniques [5]. Given the similarities between spotlight mode SAR and ISAR, these techniques ap-

ply to both processing types. He adapted techniques and theorems commonly used in computer-aided tomography, better known as CAT scans, to simplify spotlight mode processing. In particular, he described the processing in terms of the projection-slice theorem.

Jakowatz characterized the projection-slice theorem by stating that the one-dimensional (1-D) Fourier transform of a *linear projection* of the reflectivity density (the target area imaged) is equal to the 2-D Fourier transform of the reflectivity density [6]. Mathematically, the projection-slice theorem is written as

$$G(U \cos \theta, U \sin \theta) = P_{\theta}(U), \quad (2.1)$$

where G is the 2-D Fourier transform of the reflectivity density, P_{θ} is the Fourier transform on the linear projection, and θ is the angle at which the linear projection of the reflectivity density is taken. All of these functions are in the U domain, defined by a θ -rotated coordinate system in the spatial frequency domain. This equation allows the projection function (derived from the SAR pulse return) to be related to the underlying reflectivity density (the resulting SAR image). The 1-D Fourier transform of the linear projection function, p_{θ} , from the spatial (u) domain into the spatial frequency (U) domain, is

$$P_{\theta}(U) = \int_{-\infty}^{\infty} p_{\theta}(u) e^{-juU} du \quad (2.2)$$

and the 2-D Fourier transform of the reflectivity density $g(x, y)$ is

$$\begin{aligned} G(U \cos \theta, U \sin \theta) &= G(X, Y) \\ &= \int_{-\infty}^{\infty} \int_{-\infty}^{\infty} g(x, y) e^{-j(xX+yY)} dx dy. \end{aligned} \quad (2.3)$$

Jakowatz further described how a Linear Frequency Modulated (LFM) radar pulse can be used in conjunction with the projection-slice theorem to gather data

for spotlight mode images. The LFM pulse is given by

$$s(t) = \cos(\omega_0 t + \alpha t^2) \Pi\left(\frac{t}{\tau_c}\right), \quad (2.4)$$

where ω_0 is the pulse center frequency, α is the ramping constant, and Π is the rectangular envelope function that evaluates to unity between $\pm\tau_c/2$ (where τ_c is the total signal time length) and zero elsewhere.

The incident LFM pulse is scattered by the target reflectivity density g with a spatial convolution of the emitted LFM pulse with linear projections of the reflectivity density orthogonal to the direction of signal propagation. The linear projections, used to represent the simultaneous sampling of reflectivity density along a line defined by the signal's planar wave front, are given in the spatial (u) domain as

$$p_\theta(u) = \int_{-\infty}^{\infty} g[x(u, v), y(u, v)] dv. \quad (2.5)$$

where u and v are defined by $x = u \cos \theta$ and $y = v \sin \theta$. This relationship is shown in Fig. 2.2. The LFM pulse return is then written as

$$r_\theta(t) = A \left\{ \int_{-u_1}^{u_1} p_\theta(u) s\left(t - \frac{2(R+u)}{c}\right) du \right\} \quad (2.6)$$

where A is an attenuation constant due to distance, R is the distance to the reflectivity density center, c is the speed of light, the LFM pulse $s(t)$ is given by Eqn. (2.4), and the integration limits represent the cross range extent of the linear projection.

The LFM pulse return, Eqn. (2.6), is deramped after reception. Deramping is a process where the incoming signal, in this case the radar return, is quadrature demodulated (to I and Q channels) and low pass filtered. The deramped channels are then recombined into one signal. The first step to deramping is to mix the received signal with inphase and quadrature signals delayed to match the two-way

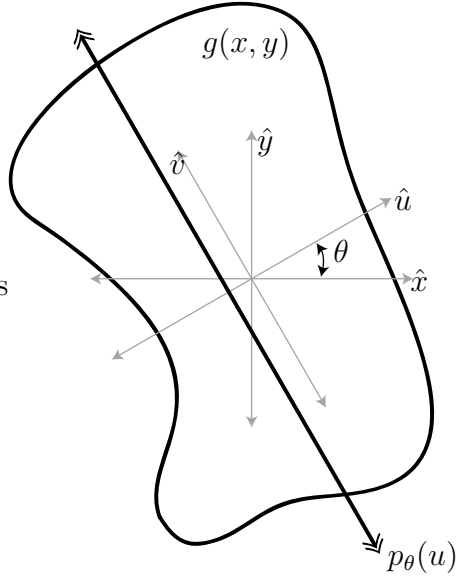


Figure 2.2: An illustration of the linear projection $p_\theta(u)$ on a θ -rotated (u, v) coordinate system over a reflectivity density $g(x, y)$.

propagation time of the received signal. The inphase mixing term is given by

$$c_I(t) = \cos \left[\omega_0 \left(t - \frac{2R}{c} \right) + \alpha \left(t - \frac{2R}{c} \right)^2 \right] \quad (2.7)$$

and the quadrature mixing term is

$$c_Q(t) = \sin \left[\omega_0 \left(t - \frac{2R}{c} \right) + \alpha \left(t - \frac{2R}{c} \right)^2 \right]. \quad (2.8)$$

Mixing each these terms with the received signal in Eqn. (2.6) and utilizing the trigonometric identities

$$\cos A \cos B = \frac{1}{2} [\cos(B - A) + \cos(A + B)] \quad (2.9)$$

$$\cos A \sin B = \frac{1}{2} [\sin(B - A) + \sin(A + B)] \quad (2.10)$$

results in processed signals given by

$$\begin{aligned} \tilde{r}_{\theta,I}(t) &= \frac{A}{2} \Re \left\{ \int_{-u_1}^{u_1} p_{\theta}(u) \left[e^{j \left[\omega_0 \frac{2u}{c} + \alpha \left(t - \frac{2R}{c} \right)^2 - \alpha \left(t - \frac{2(R+u)}{c} \right)^2 \right]} \right. \right. \\ &\quad \left. \left. + e^{j \left[2\omega_0 \left(t - \frac{2R}{c} - \frac{u}{c} \right) + \alpha \left(t - \frac{2R}{c} \right)^2 + \alpha \left(t - \frac{2(R+u)}{c} \right)^2 \right]} \right] \right. \\ &\quad \left. \Pi \left(\frac{t - 2(R+u)/c}{\tau_c} \right) du \right\} \end{aligned} \quad (2.11)$$

and

$$\begin{aligned} \tilde{r}_{\theta,Q}(t) &= \frac{A}{2} \Im \left\{ \int_{-u_1}^{u_1} p_{\theta}(u) \left[e^{j \left[\omega_0 \frac{2u}{c} + \alpha \left(t - \frac{2R}{c} \right)^2 - \alpha \left(t - \frac{2(R+u)}{c} \right)^2 \right]} \right. \right. \\ &\quad \left. \left. + e^{j \left[2\omega_0 \left(t - \frac{2R}{c} - \frac{u}{c} \right) + \alpha \left(t - \frac{2R}{c} \right)^2 + \alpha \left(t - \frac{2(R+u)}{c} \right)^2 \right]} \right] \right. \\ &\quad \left. \Pi \left(\frac{t - 2(R+u)/c}{\tau_c} \right) du \right\}, \end{aligned} \quad (2.12)$$

where \Re and \Im take the real or imaginary parts of the integral, respectively, to extract the appropriate sine or cosine terms. The tilde (\sim) on the received signals denotes the received signals have been changed by processing.

The next deramping step is low pass filtering. Low pass filtering these two mixed signals removes the second exponential term, the sum term in Eqns. (2.9) and (2.10). Slightly rearranging the first exponential term allows writing the low pass filtered signals as

$$\tilde{r}_{\theta,I}(t) = \frac{A}{2} \Re \left\{ \int_{-u_1}^{u_1} p_{\theta}(u) e^{j \left[-\alpha \left(\frac{2u}{c} \right)^2 + \left(\frac{2u}{c} \right) \left(\omega_0 + 2\alpha \left(t - \frac{2R}{c} \right) \right) \right]} \Pi \left(\frac{t - 2(R+u)/c}{\tau_c} \right) du \right\} \quad (2.13)$$

and

$$\tilde{r}_{\theta,Q}(t) = \frac{A}{2} \Im \left\{ \int_{-u_1}^{u_1} p_{\theta}(u) e^{j \left[-\alpha \left(\frac{2u}{c} \right)^2 + \left(\frac{2u}{c} \right) \left(\omega_0 + 2\alpha \left(t - \frac{2R}{c} \right) \right) \right]} \Pi \left(\frac{t - 2(R+u)/c}{\tau_c} \right) du \right\}. \quad (2.14)$$

These I and Q terms are then combined to form

$$\tilde{r}_\theta(t) = \frac{A}{2} \left\{ \int_{-u_1}^{u_1} p_\theta(u) e^{j[-\alpha(\frac{2u}{c})^2 + (\frac{2u}{c})(\omega_0 + 2\alpha(t - \frac{2R}{c}))]} \Pi\left(\frac{t - 2(R+u)/c}{\tau_c}\right) du \right\}. \quad (2.15)$$

Ignoring the first term in the exponential, $-\alpha(\frac{2u}{c})^2$, and attributing it to skew allows rewriting Eqn. (2.15) as

$$\tilde{r}_\theta(t) = \frac{A}{2} \left\{ \int_{-u_1}^{u_1} p_\theta(u) e^{j[\frac{2u}{c}(\omega_0 + 2\alpha(t - \frac{2R}{c}))]} \Pi\left(\frac{t - 2(R+u)/c}{\tau_c}\right) du \right\}. \quad (2.16)$$

This equation can now be recognized as the Fourier transform of p_θ , and can be rewritten as

$$\tilde{r}_\theta(t) = \frac{A}{2} P_\theta \left\{ \frac{2}{c} \left(\omega_0 + 2\alpha \left(t - \frac{2R}{c} \right) \right) \right\} \quad (2.17)$$

$$= \frac{A}{2} P_\theta(U) \quad (2.18)$$

where t has been time limited by Π . The effect of this time limiting is discussed below. By Eq. 2.17, the spatial frequency U domain maps to the time domain as

$$U = \frac{2}{c} \left(\omega_0 + 2\alpha \left(t - \frac{2R}{c} \right) \right) \quad (2.19)$$

where t is again time limited by Π .

According to the projection slice theorem shown in Eqn. (2.1), P_θ represents a linear trace through G (the 2-D Fourier transform of the reflectivity density). Since, the U domain is a θ -rotated version of the spatial frequency domain, the deramped return can be viewed per the projection slice theorem as

$$\tilde{r}_\theta(t) = \frac{A}{2} G(X, Y) \quad (2.20)$$

$$= \frac{A}{2} G(U \cos \theta, U \sin \theta). \quad (2.21)$$

Each processed return, at a unique θ , traces a spoke into $G(U \cos \theta, U \sin \theta)$. Multiple returns at different θ values form a disc sector G . Time limiting the return $r_\theta(t)$ constrains the disc to an annulus, where annulus width is proportional to LFM pulse bandwidth and the offset is proportional to the center pulse frequency. This relationship is illustrated in Fig. 2.3.

From $G(U \cos \theta, U \sin \theta)$, the 2-D Fourier transform of the reflectivity density, a SAR image can be reconstructed by a 2-D *inverse* Fourier transform. Since $G(U \cos \theta, U \sin \theta)$ is sampled on the polar grid naturally defined by the spokes shown in Fig. 2.3, a polar to rectangular interpolation is usually performed. This interpolation then allows Fast Fourier Transform (FFT) use. The 2-D inverse Fourier transform projects the data from the spatial frequency (U) domain to the image (u) domain, defined in range and cross range.

2.3.1 Bandwidth. Bandwidth defines the total frequency change the target is illuminated through. Usually measured in Gigahertz (GHz), the bandwidth directly determines the ISAR image range resolution. This range resolution δ_{range} is found from

$$\delta_{\text{range}} = \frac{c}{2B}, \quad (2.22)$$

where c is the speed of light, B is the propagated signal bandwidth, and δ_{range} is the ISAR image range resolution.

Since bandwidth is inversely proportional to resolution, a more detailed image can generally be generated using a higher bandwidth. Frequency *extent* determines the width of the spatial frequency arc shown in Fig. 2.3, and *both* frequency increment and bandwidth together define the number of frequencies that are considered for each target aspect.

The bandwidth maps to the spatial frequency annulus shown in Fig. 2.3 as

$$\text{annulus width} = \frac{4\pi B}{c}, \quad (2.23)$$

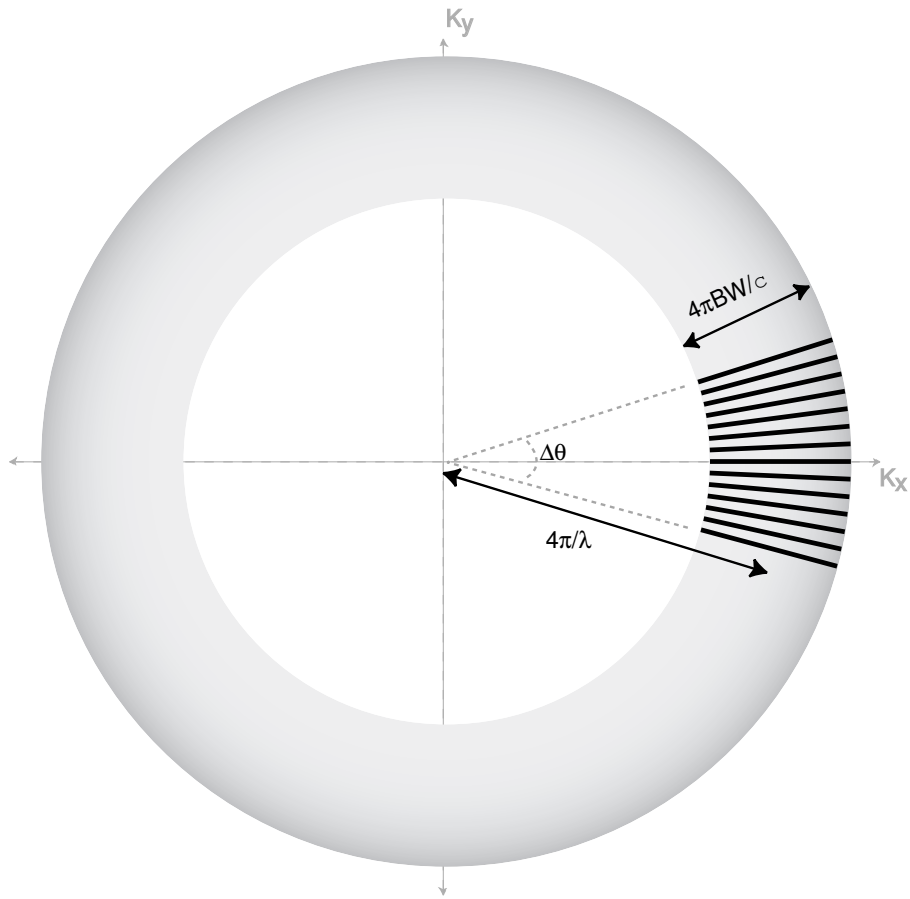


Figure 2.3: Spotlight data gathered in spatial frequency space. The angle of the data in spatial frequency is the same as the angle at which the data is physically collected. Annulus width is proportional to the radar pulse bandwidth, and offset is proportional to pulse center frequency.

where B is the bandwidth of the signal *in Hz*, and c is the speed of light. This mapping corresponds to Eqn. 2.19, where the second term determines the annulus width and can therefore be written as

$$\text{annulus width} = \frac{2}{c} \left(2\alpha \left(t - \frac{2R}{c} \right) \right) \Bigg|_{t=-\frac{\tau_c}{2} + \frac{2(R+u)}{c}}^{t=\frac{\tau_c}{2} + \frac{2(R+u)}{c}} \quad (2.24)$$

$$= \frac{4\alpha}{c} \left(\frac{\tau_c}{2} + \frac{2(R+u)}{c} - \frac{2R}{c} \right) - \frac{4\alpha}{c} \left(-\frac{\tau_c}{2} + \frac{2(R+u)}{c} - \frac{2R}{c} \right) \quad (2.25)$$

$$= \frac{4}{c} (\alpha\tau_c) \quad (2.26)$$

$$= \frac{4}{c} (\pi B) \quad (2.27)$$

$$= \frac{4\pi B}{c}, \quad (2.28)$$

where t is evaluated at its Π extents and the bandwidth B is related to the pulse ramping constant α by $B = (\alpha/\pi)\tau_c$ [7].

2.3.2 Frequency Center. The frequency center defines the midpoint, in frequency, of the signal illuminating the target. This frequency center also determines how far the spatial frequency arc, shown in Fig. 2.3, is displaced from the origin. The higher the frequency center, the shorter the wavelength propagated towards the target.

The frequency center maps to the spatial frequency annulus shown in Fig. 2.3 as

$$\text{annulus midpoint} = \frac{4\pi}{\lambda_0}, \quad (2.29)$$

where λ_0 is the mean (or center) pulse wavelength. This mapping corresponds to Eqn. 2.19, where ω_0 is the frequency center and

$$\text{annulus midpoint} = \frac{4\pi}{\lambda_0} \quad (2.30)$$

$$= 2\frac{2\pi}{\lambda_0} \quad (2.31)$$

$$= 2\frac{\omega_0}{c} \quad (2.32)$$

$$= \frac{2}{c}\omega_0. \quad (2.33)$$

The first term in Eqn. 2.19 thus determines the midpoint of the annulus, and relates to the frequency center.

2.3.3 Frequency Increment. Since returned signal frequencies are discretely sampled, the frequency increment defines the separation between consecutive signal frequencies. The frequency increment also defines the total range extent of the resulting ISAR image as

$$\Delta_{\text{range}} = \frac{B}{\delta_f}\delta_{\text{range}} \quad (2.34)$$

$$= \frac{c}{2\delta_f}, \quad (2.35)$$

where δ_f is the frequency increment, B is the bandwidth in Hz, and Δ_{range} is the total ISAR image range extent. Frequency increment and bandwidth together define the number of frequencies the received signal is evaluated for. Each frequency thus has a returned magnitude and phase associated with it.

2.3.4 Angular Span. The angular span defines the angle over which the radar illuminates the target. The angular span is equal to the angular span of the spatial frequency arc, Fig. 2.3, extends. Assuming a narrowband signal, the angular

span affects the resulting ISAR image resolution as

$$\delta_{\text{crossrange}} = \frac{\lambda_0}{2\Delta_\theta}, \quad (2.36)$$

where λ_0 is the *mean* or center propagated signal wavelength, Δ_θ is the total angle span the signals are propagated from, and $\delta_{\text{crossrange}}$ is the resulting cross range resolution. Angular increment and angular span together determine the number of aspects from which a signal must be propagated towards a target.

2.3.5 Angular Increment. Angular increment defines the separation, in angle, between consecutive propagation locations. The angular increment defines regular intervals inside the total angular span defined by Sec. 2.3.4 from which signal frequencies (set by the frequency span and center of Secs. 2.3.1 and 2.3.2) are propagated. The resulting ISAR image's cross range extent $\Delta_{\text{crossrange}}$ is

$$\Delta_{\text{crossrange}} = \frac{\Delta_\theta}{\delta_\theta} \delta_{\text{crossrange}} \quad (2.37)$$

$$= \frac{\lambda_0}{2\delta_\theta}, \quad (2.38)$$

where δ_θ is the angular increment, Δ_θ is the total angular span, and λ_0 is the *average* or center wavelength of the propagated signal. Given an angular center, angular increment and angular span determine the aspects from which signals are propagated towards the target.

2.4 SBR and ISAR Interaction

Xpatch[®] uses SBR to calculate the scattered fields from a given set of aspects and illumination frequencies. The scattered fields are used by the ISAR processing algorithm to generate the appropriate ISAR image. While the SBR and ISAR processing algorithms are distinct, the parameters of each can affect the behavior of the other. This section describes the interaction between SBR and ISAR when

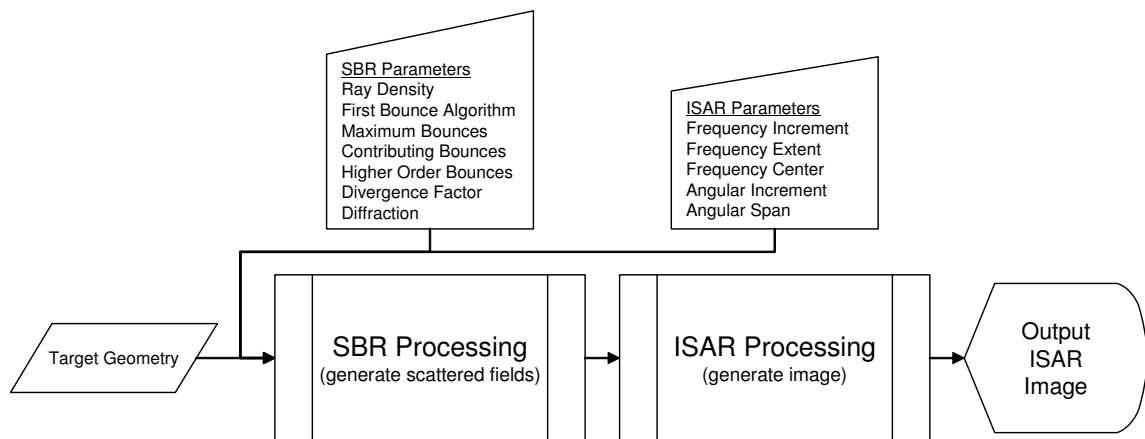


Figure 2.4: The process that Xpatch[®] uses to generate an ISAR image starts with the definition of target geometry, SBR-specific parameters, and ISAR-specific parameters. This data feeds into the SBR process, which generates the scattered fields at the specified aspects and frequencies. The scattered fields are then processed into an ISAR image.

Xpatch[®] generates an ISAR image from the parameters specified in Secs. 2.2 and 2.3. An illustration of SBR and ISAR process and parameter interaction is shown in Fig. 2.4. While both SBR and ISAR parameters influence the final scattered fields and resulting ISAR images, only SBR parameters change the SBR algorithm’s inherent behavior.

Parameters specific to SBR, covered in Sec. 2.3, propagate directly through the ISAR process. Each parameter influences the calculated scattered field. Since the scattered field is input to the ISAR image generation process, these parameters affect the final ISAR image.

Parameters specific to ISAR, covered in Sec. 2.3, form the requirements dictating the aspect and frequency set from which the SBR technique is applied. Although they affect the application of the SBR algorithm, the SBR algorithm itself is not altered.

2.4.1 Ray Density. Ray density, described in Sec. 2.2.1, affects the scattered field calculation by reflecting at specific points over the target geometry. In

true EM scattering, the incident wave is usually described as a continuous plane wave over the entire target¹. However, the inherent discretization of ray tubes in the SBR technique is only an approximation of an incident plane wave. The incident ray tubes impinge discrete points on the target geometry. The ray tubes then successively reflect onto another set of discrete points on the geometry until they are reradiated into free space. A different incident aspect angle produces a different set of initial reflection points. This different initial reflection point sets can result in dramatically different reflection angles, greatly impacting the final scattered field and the resulting ISAR image.

The scattered field maps into the spatial frequency domain for ISAR processing and is then Fourier transformed, producing the final image. Sharp variances with respect to aspect in the spatial frequency domain are synonymous with frequency content throughout the Fourier transformed image domain. Since the polar to rectangular interpolation performed before the Fourier transform substantially preserves discontinuities, any discontinuities in the spatial frequency angular direction result in image content spread throughout the cross range extent of the resulting ISAR image. This content is in the same range bin as the discontinuity that caused it. Aspect dependent discontinuities have a greater effect on cross range image content than range content due to mapping constant aspect frequency sweeps along annulus spokes (as in Fig 2.3).

Aspect-based discontinuities due to the inherent shooting grid discretization are most pronounced for geometries formed of shapes changing significantly with respect to angle. For example, a cavity produces a dramatically different scattered field with a small incident aspect change. This result occurs due to the large number of reflections the small change in initial reflection points propagates through. Similarly, a target geometry with sharp edges produces a dramatically different set

¹This description is of course also an approximation, relying on the assumption that the target is completely enclosed within a quiet zone where the incident spherical wave is locally planar

of initial reflection points with a small change in incident aspect, attributed to the incident ray reflecting on opposite sides of the edge as the aspect changes. The ray tube then continues until finally reflected off geometry. The final reflection point may be significantly displaced from the last reflection point of the same ray tube at the previous aspect. A flat plate, on the other hand, does not change the initial incident reflection points much based on a small change in incident aspect. Therefore, the resulting scattered field changes are minimal.

2.4.2 Angular Increment. Angular increment, described in Sec. 2.3.5, is a parameter that determines the final ISAR image's cross range dimension. Decreasing the aspect increment results in smaller aspect changes between each subsequent SBR ray shoot. Aspect increment does not affect the SBR process itself, but it does affect the incident aspect locations where SBR is applied. Therefore, any change in aspect increment alone does not affect the scattered field calculation; each calculation is independently applied. However, aspect increment variation does have a significant affect on the final ISAR image. The smaller the aspect increment, the more spokes are present in the spatial frequency domain. This increased spatial frequency resolution results a higher rectangularly resampled resolution and leads to a correspondingly higher cross range image extent.

2.4.3 Angular Span. Angular span, described in Sec. 2.3.4 and used with the angular increment parameter, determines the discrete set of angles where the incident SBR rays are propagated. While the angular span controls the final ISAR image cross range resolution, it does nothing to inherently change the SBR algorithm behavior. The SBR algorithm is simply applied over an aspect defined in part by angular span.

2.4.4 Frequency Center. Frequency center, described in Sec. 2.3.2 and used in combination with frequency increment and bandwidth to determine the discrete

frequency set the SBR calculated scattered fields are evaluated. Once the points of reflection and path lengths are calculated for a given aspect, the scattered fields are evaluated in closed form for each frequency. Altering the frequencies does not change the ray reflection angle or magnitude, only its resultant path length phase. Since all rays are separately propagated and the scattered fields from each propagated ray are summed in SBR, the SBR calculated total scattered field varies as a function of frequency. This variation naturally leads to variation in the final ISAR image content.

2.4.5 Frequency Increment. Frequency increment, described in Sec. 2.3.3 and used in combination with frequency center and bandwidth determines the discrete frequency set SBR calculated scattered fields are evaluated. Once the points of reflection and path lengths are calculated for a given aspect, the scattered fields are evaluated in closed form for each frequency. Therefore only one ray shoot is performed at each aspect, regardless of the number of frequencies at that aspect.

More frequencies are evaluated at each aspect as the frequency increment is reduced. This reduction causes Xpatch[®] to evaluate more scattered field values, mapped along each spoke in the spatial frequency domain. In addition to increasing the image extent of the final ISAR image, better rectangular to polar interpolation can be performed prior to the Fourier transform that creates the ISAR image.

2.4.6 Bandwidth. Bandwidth, described in Sec. 2.3.1 and used in combination with frequency center and frequency increment to determine the discrete frequency set SBR calculated scattered fields are evaluated. Since an entire ray shoot is only performed once at each aspect, increasing the bandwidth does not add ray shoots or change the performance of the SBR algorithm itself. This increase will, however, affect the final ISAR image resolution by providing a wider spatial frequency domain annulus.

2.5 Smear Assessment Algorithm

In order to measure the input parameter and geometry effects on cross range smear, a quantitative method assessing the cross range smear extent is required. This assessment algorithm mathematically generates a numerical value for the smear present in an ISAR image. This numerical smear value feeds into the analysis of parameters affecting smear in Xpatch[®] ISAR images.

Since ISAR images are essentially 2-D magnitude plots, worst case smear manifests itself as constant real-valued magnitude across the entire cross range extent. In other words, the cross range slice under examination consists of one constant value across the entire cross range. Conversely, minimum smear is a purely real delta function within the cross range slice. The delta functions represent the scattering centers of the imaged reflectivity density. Further discussion on maximum and minimum smear is given as the smear assessment algorithm is evaluated for each case.

First, a single cross range slice $g(x, y_0)$ is taken from the image. Due to ISAR image pixelization, the slice is defined discretely along x . The slice is then transformed into its frequency domain using a one dimensional Fourier transform and designated as $\tilde{G}(X, y_0)$. The result is not in a true *spatial frequency* domain since a 2-D Fourier transform is required in the image formation process, so the result is denoted \tilde{G} instead of G ,

$$\tilde{G}(X, y_0) = \mathcal{F} \{g(x, y_0)\}. \quad (2.39)$$

The absolute value of $\tilde{G}(X, y_0)$ is taken to extract its magnitude,

$$|\tilde{G}(X, y_0)| = |\mathcal{F} \{g(x, y_0)\}|, \quad (2.40)$$

and then differentiated over X as

$$\frac{d}{dx} \left\{ |\tilde{G}(X, y_0)| \right\} = \frac{d}{dx} \left\{ |\mathcal{F} \{g(x, y_0)\}| \right\}. \quad (2.41)$$

This differentiation is discrete because of the discrete nature of X , so the derivative is simply the difference between consecutive values of $|\tilde{G}(X, y_0)|$. Since cross range smear is a result of angle-based discontinuities in the spatial frequency data, this step provides an approximate measure of discontinuity.

An absolute value is again applied to force all decreases in $|\tilde{G}(X, y_0)|$, and hence all negative values of $\frac{d}{dX}|\tilde{G}(X, y_0)|$, positive. This step is applied as

$$\left| \frac{d}{dx} \left\{ |\tilde{G}(X, y_0)| \right\} \right| = \left| \frac{d}{dx} \left\{ |\mathcal{F} \{g(x, y_0)\}| \right\} \right|. \quad (2.42)$$

Now that all changes in $|\tilde{G}(X, y_0)|$ contribute positively, each value of the discrete function $\frac{d}{dX}|\tilde{G}(X, y_0)|$ is summed to produce the single smear value. This smear value can take any value in $[0, \infty)$, where minimum smear is when the function $|\tilde{G}(X, y_0)|$ is constant and maximum smear is approached when $|\tilde{G}(X, y_0)|$ has large changes/discontinuities. The smear value in each cross range slice is therefore constructed as

$$\text{smear}(y_0) = \text{sum} \left\{ \left| \frac{d}{dx} \left\{ |\tilde{G}(X, y_0)| \right\} \right| \right\} \quad (2.43)$$

$$= \text{sum} \left\{ \left| \frac{d}{dx} \left\{ |\mathcal{F} \{g(x, y_0)\}| \right\} \right| \right\}. \quad (2.44)$$

The smear value associated with the entire ISAR image is the maximum of all cross range slice smear values, or

$$\text{smear} = \max \left\{ \text{sum} \left\{ \left| \frac{d}{dx} \left\{ |\tilde{G}(X, y_0)| \right\} \right| \right\} \right\} \quad (2.45)$$

$$= \max \left\{ \text{sum} \left\{ \left| \frac{d}{dx} \left\{ |\mathcal{F} \{g(x, y_0)\}| \right\} \right| \right\} \right\}. \quad (2.46)$$

2.5.1 Analysis of Maximum Smear. Extensive smear in a magnitude ISAR image is a constant real-valued slice extending the entire cross range length. Further, maximum smear is present when the smear is constant over an ISAR image infinite in cross range extent. The constant cross range slice is then denoted as

$$g(x, y_0) = C. \quad (2.47)$$

Its Fourier transform is a purely real delta function,

$$\mathcal{F} \{C\} = C\delta(X). \quad (2.48)$$

Taking the absolute value has no effect since everything is already positive, so

$$|\mathcal{F} \{C\}| = |C\delta(X)| \quad (2.49)$$

$$= C\delta(X). \quad (2.50)$$

The derivative of this function, implemented as the difference between consecutive discrete X values, is

$$\frac{d}{dx} |\mathcal{F}\{C\}| = |C\delta(X)| \quad (2.51)$$

$$= \frac{d}{dx} C\delta(X) \quad (2.52)$$

$$= \begin{cases} \infty & X = 0- \\ -\infty & X = 0+ \\ 0 & \text{else} \end{cases} \quad (2.53)$$

where the infinite values are located at the intervals $(-\delta_X, 0)$ and $(0, \delta_X)$ given the X resolution δ_X . Another absolute value ensures all the derivatives are positive, in order to constructively contribute to the sum. The above result then becomes

$$\left| \frac{d}{dx} |\mathcal{F}\{C\}| \right| = \begin{cases} \infty & X = 0- \\ \infty & X = 0+ \\ 0 & \text{else.} \end{cases} \quad (2.54)$$

The summation over all X , defined as the smear in this cross range slice with maximum smear, approaches infinity.

As a practical example, the Matlab[®]-implemented cross range smear algorithm is tested on a unity constant over a 2500 sample cross range slice. This input function is shown in Fig. 2.5. In this case, the algorithm assesses a 13440 smear value.

2.5.2 Analysis of Minimum Smear With Single Point Scatterer. A reflectivity density can generally be decomposed into a discrete and independent point scatterer set, called scattering centers [8]. These scattering centers are ideally represented in an ISAR image as delta functions in range and cross range. Therefore, an ISAR image without smear is a discrete 2-D delta function set. Each delta function represents a scattering center of the reflectivity density being imaged.

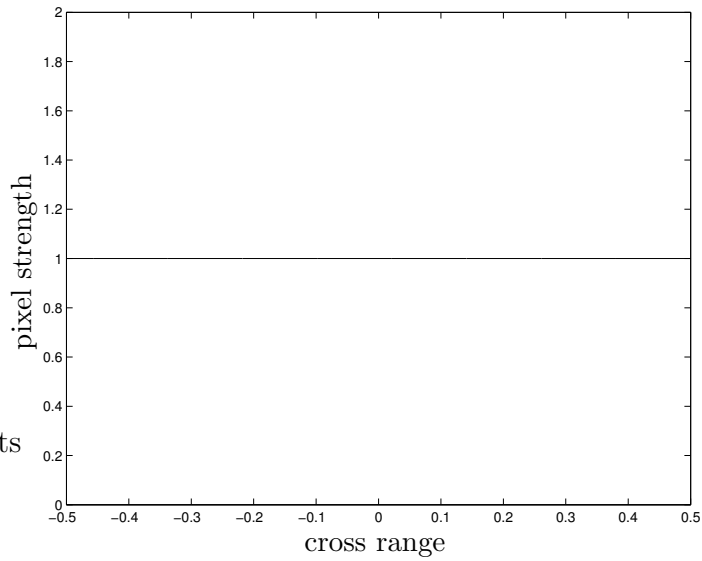


Figure 2.5: A cross range smear slice with maximum smear, using 2500 cross range pixels, generates a 13440 smear value.

A single scattering center illustrates a best case scenario, an ISAR image without smear. Since this single point scatterer is shown as a delta function in the ISAR image domain and the ISAR image presents no phase information, the scattering center is given as a delta function located at x_n scaled by a purely real constant C . As the image is analyzed over each cross range slice, assumed infinite in extent, the scattering center presents itself as

$$g(x, y_0) = C\delta(x - x_n). \quad (2.55)$$

Its Fourier transform is a purely real constant appropriately frequency shifted,

$$\mathcal{F}\{C\delta(x)\} = Ce^{-jx_nX}. \quad (2.56)$$

where X is finite in extent and discretely sampled. Taking the magnitude of this value strips off the complex exponential,

$$|\mathcal{F}\{C\delta(x)\}| = |Ce^{-jx_nX}| \quad (2.57)$$

$$= C. \quad (2.58)$$

The derivative of this constant is zero for all discrete values of X ,

$$\frac{d}{dx} |\mathcal{F}\{C\delta(x)\}| = \frac{d}{dx} C \quad (2.59)$$

$$= 0. \quad (2.60)$$

This result is summed over all X to produce a smear value for a single point scatterer of identically zero.

As a practical example, the Matlab[®] implemented cross range smear algorithm was tested on a single delta functions of unity strength displaced 70% down a cross range slice with 2500 samples. This input function is shown in Fig. 2.6. In this case, the algorithm assesses a smear value of 4.19e-13.

2.5.3 Analysis of Minimum Smear With Multiple Point Scatterers. The result for minimum smear can be generalized for a discrete set of independent point scatterers along the cross range slice. This set represents an accurate point scatterer decomposition of a reflectivity density imaged into a magnitude-only ISAR plot as a set of real delta functions arbitrarily placed along the cross range slice. The corresponding reflectivity density is given by

$$g(x, y_0) = \sum_n C_n \delta(x - x_n), \quad (2.61)$$

where x_n is the spatial location and C_n is the positive magnitude of delta function n . The cross range extent is assumed infinite. Its Fourier transform is the sum of

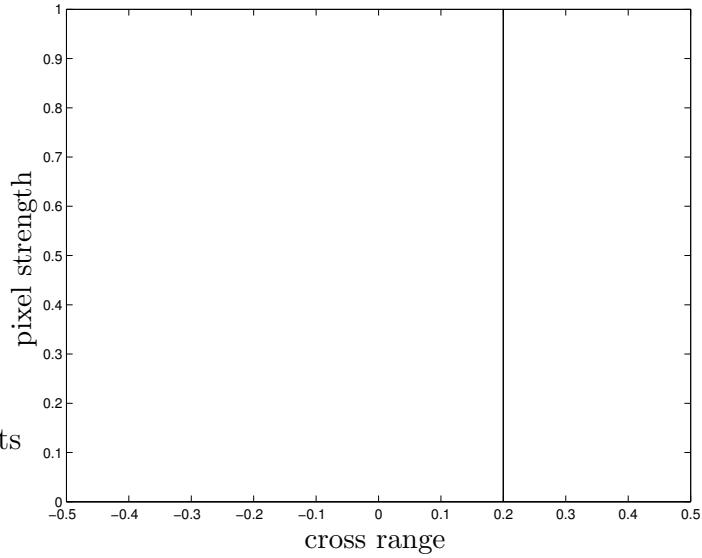


Figure 2.6: A single delta function displaced 20% from the center of a 2500 pixel cross range slice generates a smear value of 4.19e-13.

frequency-shifted constants,

$$\mathcal{F} \left\{ \sum_n C_n \delta(x - x_n) \right\} = \sum_n C_n e^{-jx_n X}, \quad (2.62)$$

where X is discretely sampled and finite in extent. Taking the magnitude of this value removes the phase of the result. However, since the complex exponentials constructively and destructively interfere, the magnitude will smoothly vary within bounds set by $[0, \sum^n C_n]$. This step is shown as

$$\left| \mathcal{F} \left\{ \sum_n C_n \delta(x - x_n) \right\} \right| = \left| \sum_n C_n e^{-jx_n X} \right|. \quad (2.63)$$

The variation between consecutive points of Eqn. (2.63) will depend on the number of point scatterers n and their position in the cross range slice x_n . The greater n is, the sharper variation between consecutive points in Eqn. (2.63) can be.

The derivative of Eqn. 2.63 is the difference between values at consecutive points along X . The value at each point along X of this derivative will depend on

n and x_n . However, since the differentiated function is the sum of sinusoids and therefore without large discontinuities, the difference between consecutive points in Eqn. (2.63) is kept small (but non-zero).

Taking an absolute value ensures that all discontinuities are represented by positive numbers. This result is then summed over the X extent to cumulatively measure all discontinuities. Since each difference is relatively small, their sum will be much less than an otherwise identical maximum smear case. In the maximum smear case, dramatic discontinuities contribute very large differences to the summation.

As a practical example, the Matlab[®] implemented cross range smear algorithm was tested on three delta functions of varying strength placed arbitrarily along a cross range slice with 2500 samples. This input function is shown in Fig. 2.7. In this case, the algorithm assesses a smear value of 2513. This number is much less than the 13440 computed for the maximum smear case of Fig. 2.5.

Another example is shown in Fig. 2.8. Here, five delta functions of varying strength are placed arbitrarily along the same cross range slice. This function has a smear value of 3019, which is still significantly less than the 13440 computed for maximum smear.

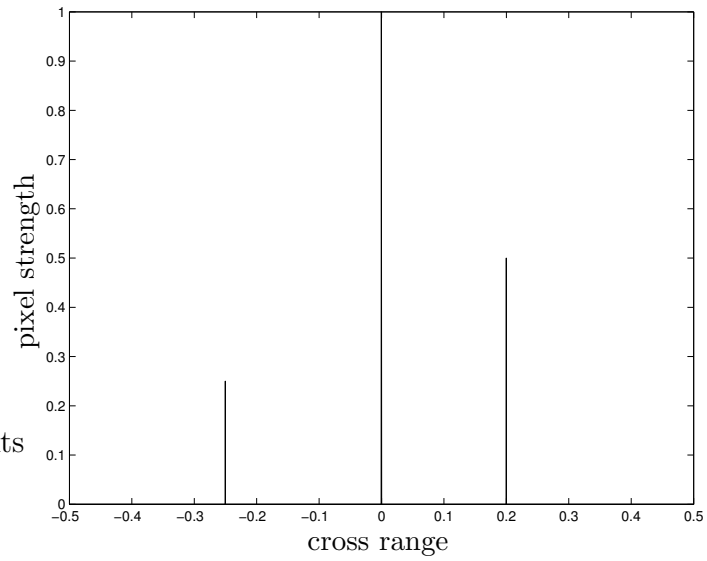


Figure 2.7: Three delta functions placed along a cross range slice of 2500 samples have a smear value of 2513.

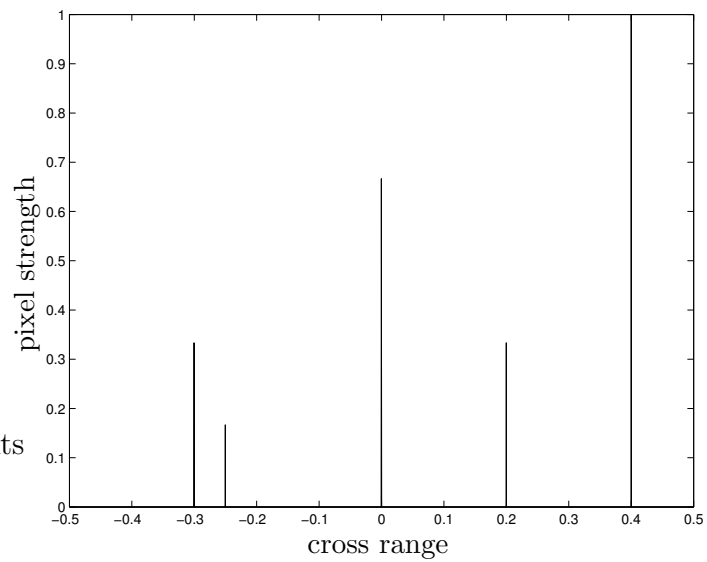


Figure 2.8: Five delta functions placed along a cross range slice of 2500 samples have a smear value of 3019.

III. Methodology

3.1 Introduction

This chapter presents the methodologies used to perform two tasks: characterize cross range smear and analyze the smear reduction method presented by Bhalla and Ling [2]. The smear characterization is given in terms of the geometries and input parameters used by Xpatch[®] when generating Inverse Synthetic Aperture Radar (ISAR) images. The smear reduction implementation and analysis methodology is then described, building upon the smear characterization work.

Cross range smear, present in Xpatch[®] ISAR images and the subject of characterization, is a product of scattered fields generated through Xpatch[®]'s Shooting and Bouncing Rays (SBR) implementation. Chapter II describes the SBR technique and ISAR image generating process. The methodology characterizing cross range smear is separated into the following tasks.

1. Identify parameters potentially affecting cross range smear.
2. Analytically describe how parameters affect cross range smear.
3. Define scattering targets with geometries inducing a variety of scattering mechanisms.
4. Define a set parameter values and target geometries, used to generate Xpatch[®] ISAR images, that allows important cross range smear factors to be extracted and identified.
5. Generate Xpatch[®] ISAR images with chosen targets and variable parameters.
6. Analyze the factors (parameters and geometries) affecting cross range smear in the resulting Xpatch[®] ISAR images.

The parameters affecting SBR and subsequent ISAR image generation were previously defined and individually discussed in Secs. 2.2 and 2.3. Section 2.4 further

discusses these parameters in terms of their interaction with the SBR/ISAR process and potential for affecting cross range smear.

The scattering targets and parameter extents discussed in this chapter are used to generate Xpatch[®] ISAR images. Section 3.2 describes the various targets used to generate each ISAR image set. For each scattering target, an ISAR image set is generated by varying previously identified parameters. Section 3.3 identifies the specific parameter values and ranges. A Design of Experiments (DOE) approach is used to construct an ISAR image set using specific parameter values facilitating an empirical cross range smear analysis as a function of those input parameters. Section 3.4 describes the DOE analysis approach while Chap. IV presents the results of this analysis.

This chapter also discusses the implementation of the method presented by Bhalla and Ling [2] to reduce cross range smear. Section 3.5 describes how the smear reduction is implemented and how the subsequent smear analysis is performed. Chapter V presents the results of this analysis. In addition to the smear reduction technique as proposed by Bhalla and Ling, a slightly modified version is presented.

Xpatch[®] version 4.7.16 is used for all scattered field computation and ISAR image generation.

3.2 Target Geometries

This section identifies target models used by Xpatch[®] along with parameters defined in Sec. 3.3 when calculating the scattered fields. ISAR images are generated from these scattered fields and then analyzed for cross range smear presence. These targets are Computer-Aided Design (CAD) models, each with geometric features affecting electromagnetic (EM) scattering. This scattering forms the foundation for the ISAR imaging process, therefore careful geometry selection is extremely important. The targets chosen are also of varying complexity, generally divided into two groups: canonical and moderately complex targets.

Table 3.1: The target geometries exercise a variety of scattering mechanisms in Xpatch[®] while generating scattered field data and the resulting ISAR image.

Geometry Name	Category	Type
Flat Rectangular Plate	Specular	Canonical
Ridged Plate	Edge	Moderately Complex
Slicy	Multiple	Moderately Complex

Canonical shapes provide one dominant scattering mechanism, such as specular reflection, edge diffraction, or multiple (2-3) bounce reflections. Moderately complex targets possess several scattering mechanisms affecting the resultant scattered field, such as cavity-type multiple bounce reflections or additional diffraction components. A table of the target geometries used is given in Table 3.1.

Each geometry file is described in one of two CAD formats: IGES or facet. An IGES file exactly describes curved surfaces while a facet file describes flat triangular facets that, at best, approximate a curved surface. Each respective section specifies the CAD file format used for each geometry.

Diffraction due to geometric edges is defined in Xpatch[®] by a separate (.edge) file. This file identifies diffraction-inducing straight lines of the CAD geometry. Since diffraction is not considered in purely SBR calculated scattering, the diffractive edges' scattering contribution is only added to the primary SBR scattering when the parameter to include diffraction effects, Sec. 3.3.1.3, is enabled.

Other common scattering mechanisms, such as creeping and traveling waves, are not modeled due to the nature of the SBR high frequency assumptions and application.

All target geometries are imaged with a waterline ISAR aperture. The SAR aperture, or the collection of imaging aspects defined by its angular span and angular increment, is thus set along zero degrees elevation and sweeps out an angular span centered about zero degrees azimuth (centered on the x-axis) as illustrated by Fig. 3.1.

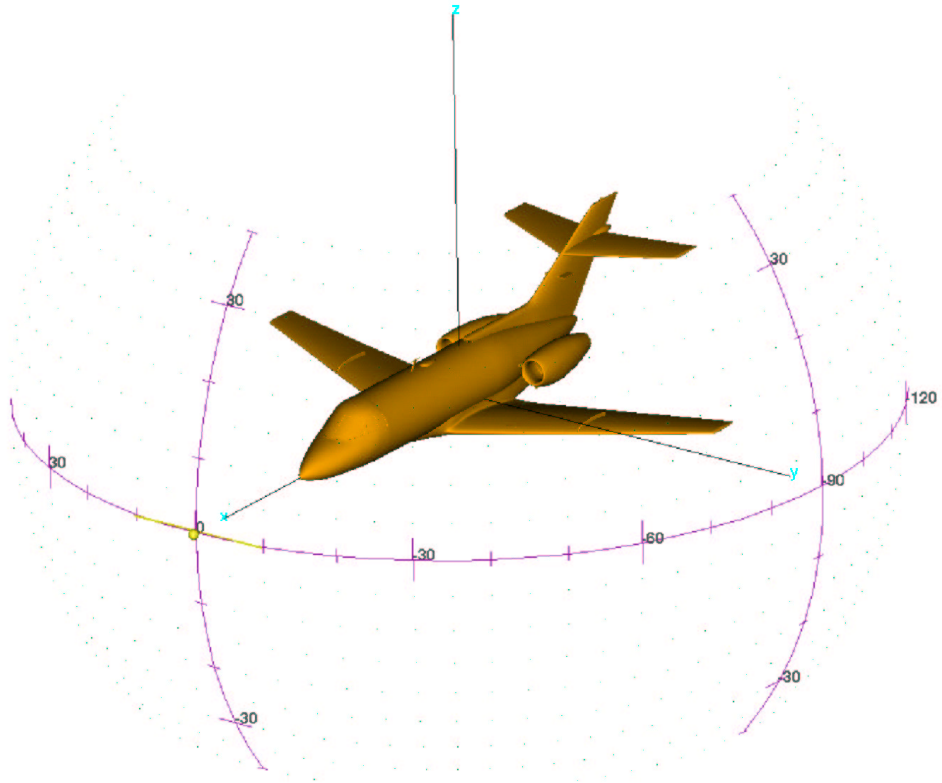


Figure 3.1: An illustration of a waterline ISAR aperture, at zero degrees elevation and centered about zero degrees azimuth (the \hat{x} axis). The ISAR aperture in this example extends for a total angular span of twenty degrees. All ISAR images generated for geometries in Sec. 3.2 use this general orientation.

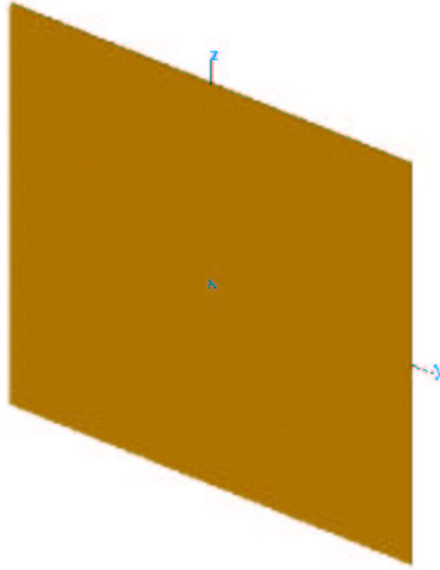


Figure 3.2: The flat rectangular plate geometry induces primarily single-bounce specular scattering.

3.2.1 Flat Rectangular Plate. The flat rectangular plate geometry shown in Fig. 3.2 is a 100 inch by 100 inch plate normal to the \hat{x} axis, with a uniform thickness of 1 inch. As a primarily specular geometry, the effects due to SBR application are exclusively single bounce reflections. Diffraction along all 12 edges, 4 on each side plus 4 due to the width, is also present. However, diffraction is secondary to the primary specular scattering.

The flat rectangular plate serves as a canonical shape that examines the SBR and ISAR interactions due to primarily specular scattering. It is specified as an IGES file.

3.2.2 Ridged Plate. The ridged plate geometry shown in Fig. 3.3 is a flat rectangular plate with triangular ridges over the entire $+\hat{x}$ surface, extending in the \hat{z} direction. The 1 inch thick base plate is 100 inches by 100 inches in extent. Each ridge is an additional 10 inches from base to tip and is 10 inches along each base for

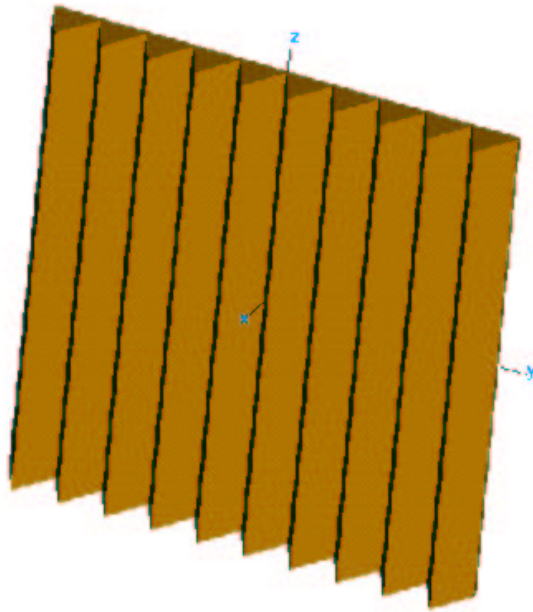


Figure 3.3: The ridged plate geometry is a flat plate with triangular ridges facing in the positive \hat{x} direction. It is mostly a single and double bounce scattering geometry with edge diffraction along the edges of the base plate and on the top of each ridge. The ridges are meant to excite a large angular reflection change and, therefore, a large change to the scattered field based on a small incident angular increment.

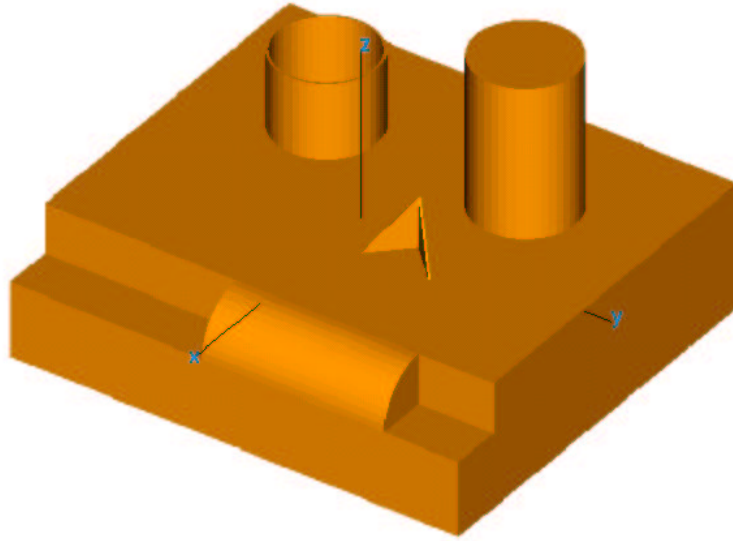


Figure 3.4: The slicy geometry is a composite of several scattering geometries including specular surfaces, singly curved surfaces, dihedrals, trihedrals, and cavities. These geometries induce specular and multiple bounce reflections, as well as diffraction along exterior edges.

a total of 10 ridges over the entire $+\hat{x}$ surface. Diffraction is due to the edges along the plate, as well as the top of each ridge. Scattering on the ridges is primarily due to single and double bounce reflections. The ridges induce dramatic changes in the ray reflections and scattered field due to a small change in incident angle.

The ridged plate is a medium complex shape that examines the SBR and ISAR interactions due to primarily low-order reflections. Those reflections vary considerably with incident angular direction. It is specified as an IGES file.

3.2.3 Slicy. The slicy geometry shown in Fig. 3.4 includes many different scattering mechanisms such as cavities, cylinders, dihedrals, trihedrals, and singly curved surfaces. Its extents are defined by a bounding box that is 96 inches along the

\hat{x} direction, 108 inches in the \hat{y} direction, and 66 inches in the \hat{z} direction. Diffraction is from all exterior edges with a wedge (interior) angle of 90 degrees.

The slicy geometry is a medium complex shape that examines SBR and ISAR interactions. This geometry induces many different scattering mechanisms. It is specified as a facet file, so ray divergence is ignored and all curved surfaces are facetized.

3.3 Parameters

Xpatch[®] generates scattered field data and the resulting ISAR image using a set of input parameters along with a specified target geometry. This section discusses the parameter values used to generate ISAR images that are analyzed for cross range smear.

Each parameter is either varied or held constant. Those that are varied, identified and discussed in Chap. II, potentially affect cross range smear in the output ISAR images. The value ranges for each of these variable parameters are discussed and justified in Sec. 3.3.1. Xpatch[®] needs additional parameters to produce ISAR images, but these do not necessarily influence cross range smear. These parameters are held constant for all ISAR images and are discussed and justified in Sec. 3.3.2.

3.3.1 Variable Parameters. This section presents the parameters varied when producing the ISAR image set. This image set is then analyzed for cross range smear. Table 3.2 presents a succinct variable parameter list. Continuous parameters may take any value between the given maximum and minimum extent while nominal parameters cycle between explicitly declared values. These values constitute the extent the parameters are allowed vary over in the course of cross range smear analysis.

3.3.1.1 Ray Density. Ray density, analytically discussed in Sec. 2.2.1, is a continuously variable parameter. It is constrained to vary between 5 and 20

Table 3.2: Variable Parameters

Parameter	Values	Units	Range Type
Ray Density	5-20	Rays/ λ	Continuous
First Bounce Algorithm	PO,SBR	N/A	Nominal
Diffraction	yes,no	N/A	Nominal
Bandwidth	1-10	GHz	Continuous
Frequency Center	10-15	GHz	Continuous
Frequency Increment	0.005-0.01	GHz	Continuous
Angular Span	5-20	degrees	Continuous
Angular Increment	0.01-0.1	degrees	Continuous

rays/ λ . The Xpatch[®] default is 10 rays/ λ , so a factor of two is used to define the maximum and minimum ray density values.

3.3.1.2 First Bounce Algorithm. The first bounce algorithm, analytically discussed in Sec 2.2.2, is a nominally variable parameter set to either PO or SBR. A third option, Z-buffer, exists, however it is infrequently used and computationally comparable to SBR. SBR is the recommended Xpatch[®] default, while PO provides additional accuracy at the cost of computational efficiency. Therefore, both SBR and PO are possible values for this parameter.

3.3.1.3 Diffraction. Diffraction is a nominally variable parameter used by Xpatch[®] to add a diffraction effect to the the total (specular) scattered field otherwise calculated by the SBR technique. EM diffraction is separately computed using an additional geometry file defining edge presence. The diffraction component is then coherently added to the fields calculated via the SBR technique. Since EM diffraction can have a strong effect on the total scattered field, it is an important parameter to examine. The inclusion of diffraction is specified by a yes or no value.

3.3.1.4 Bandwidth. Bandwidth, analytically discussed in Sec. 2.3.1, is a continuously variable parameter. It is constrained to vary between 1 and 10 GHz.

3.3.1.5 Frequency Center. Frequency center, analytically discussed in Sec. 2.3.2, is a continuously variable parameter. It is constrained to vary between 10 and 15 GHz.

3.3.1.6 Frequency Increment. Frequency increment, analytically discussed in Sec. 2.3.3, is a continuously variable parameter. It is constrained to vary between 0.005 and 0.01 GHz.

3.3.1.7 Angular Span. Angular span, analytically discussed in Sec. 2.3.4, is a continuously variable parameter. It is constrained to vary between 5 and 20 degrees. Since angular span determines the resulting ISAR image cross range resolution, this interval allows for a sub-unit cross range resolution fine enough to distinguish smaller geometry features.

3.3.1.8 Angular Increment. Angular increment, analytically discussed in Sec. 2.3.5, is a continuously variable parameter. It is constrained to vary between 0.01 and 0.1 degrees. Since angular increment determines the cross range ISAR image extent, this interval ensures that all geometries are fully contained within the ISAR image extent.

3.3.2 Constant Parameters. This section presents the parameters held constant in the generation of each ISAR image, along with their rationale for use. Table 3.3 presents a succinct list of these constant parameters along with their appropriate values. These parameters, when combined with the variable parameters defined in Sec. 3.3.1 and a target geometry in Sec. 3.2, form the inputs Xpatch[®] needs to compute scattered fields and generate a resulting ISAR image.

3.3.2.1 Max Bounces. Max Bounces, analytically discussed in Sec. 2.2.3, is the maximum number of ray bounces a SBR ray tube can reflect through before being truncated. The Xpatch[®] default is 50. A higher value only affects situations

Table 3.3: Constant Parameters

Parameter	Value
Max Bounces	50
Contributing Bounces	all
Higher Order Bounces	Incident + Scattered Field
Divergence Factor	yes
Computational Domain	Frequency
Signature Entry Mode	SAR Image
Square Resolution	no

where an extremely large number of reflections occur, such as cavities. The scattered fields due to such reflections can usually be considered negligible. Hence, this value was left constant and unchanged.

3.3.2.2 Contributing Bounces. The contributing bounces parameter, analytically discussed in Sec. 2.2.4, is set to the Xpatch[®] recommended value of ‘all’. Due to the computations required for each reflection, computing the additional scattered field contributions from every reflection point (up to the value of Max Bounces) does not impose significant computational overhead. In addition, scattered fields are more accurately computed when all bounces are taken into account.

3.3.2.3 Higher Order Bounces. Xpatch[®] calculates the surface currents at each reflection point using the higher order bounces parameter. When the parameter is set to ‘Incident + Scattered Field’, both the incident and scattered field contributions at the reflection point, in addition to the ray tube being reflected, contribute to the surface current. This parameter setting provides the most accurate surface current calculation, and the most accurate scattered field results. The other possibility involves only including the scattered field and reflected ray tube. However, using both the incident and scattered field with the ray tube is recommended. This parameter is available when Contributing Bounces, Sec. 3.3.2.2, is set to ‘all’.

3.3.2.4 Divergence Factor. The divergence factor parameter is used by Xpatch[®] to change the cross section of each SBR ray tube based on the surface curvature at the reflection point. It is a standard GO method of compensating for surface curvature to more accurately compute the scattered field. This parameter is only applicable to IGES models, where surface curvature is defined. Facetized models do not have any surface curvature. Therefore, this parameter has no effect on those targets. Divergence factor is enabled for all cases.

3.3.2.5 Computational Domain. Xpatch[®] determines the type of scattering computations needed and the need for additional parameters (such as frequencies and aspects) using the option for selecting the computational domain in tandem with the signature entry mode in Sec. 3.3.2.6. Since cross range smear is a problem in frequency domain ISAR images, the computational domain is set to Frequency Domain.

3.3.2.6 Signature Entry Mode. Xpatch[®] determines whether the scattering computation should be done in the frequency or time domain, along with the primary scattered field file format (.ss or .si), using the signature entry mode parameter. Since cross range smear is generated through frequency domain computations, SAR Image is set as the constant value for this parameter. Selecting this value allows for the input of other necessary items, such as frequency and aspect parameters that determine ISAR image dimensions, and produces a complex field/spatial frequency (.ss) file from which an ISAR image is derived. Any other value, such as RCS or Range Profile does not produce the necessary scattering data for an ISAR image.

3.3.2.7 Square Resolution. Xpatch[®] uses the square resolution parameter to force the range and cross range resolutions to be equal. Enabling this parameter does not allow independent variation of frequency and aspect parameters

and prevents the individual parameter characterization. Therefore, square resolution is set to ‘no’ for all cases.

3.4 Cross Range Smear Characterization

With the scattering targets of Sec. 3.2 and the parameters of Sec. 3.3, a DOE approach identifies important factors contributing to cross range smear. The DOE approach generates a set of ‘runs’ [9], each varying the input parameters to produce a separate ISAR image. Each target geometry is considered separately, so each set of runs is performed for each target geometry. Once Xpatch[®] has produced the requisite ISAR image set, each image is analyzed for the existence and extent of cross range smear per Sec. 2.5. These cross range smear values are then used to extract the influence of that geometries’ input parameters. This process is repeated for each geometry, and the results form the characterization of cross range smear.

The DOE approach separates input parameters into two categories: continuous and nominal. Continuous parameters may take any value between a defined maximum and minimum while nominal parameters only take discrete values, such as ‘yes’ or ‘no’. From the output value analysis, an empirical model is built approximating the SBR and ISAR image generation process—a mathematical function that produces a smear value as a function of its input parameters. Each input parameter influences the amount of cross range smear with first, second, and higher-order effects. First-order effects are weighted parameter values, second-order effects are a weighted product of two (possibly identical) input parameters, and so on. A first-order main effects model for three parameters with interaction terms can be written as

$$\text{smear} = f(p_1, p_2, p_3) \tag{3.1}$$

$$= c_0 + c_1p_1 + c_2p_2 + c_3p_3 + c_{12}p_1p_2 + c_{13}p_1p_3 + c_{23}p_2p_3, \tag{3.2}$$

where p is an input parameter and c is the corresponding weight, or coefficient. Each input parameter is normalized to vary linearly between -1 and 1. The overall number of terms (first-order, second-order, etc.) in the function equals the number of degrees of freedom (DOFs) in the model and is directly related to the number of ISAR images analyzed. The error between the Xpatch[®] SBR and ISAR process and the DOE-produced model is also directly related to the DOE design and the number of ISAR images analyzed.

There are two prominent experiment design types within the DOE framework: full and fractional factorial. A full factorial design analyzes 2^n runs by testing all combinations of high and low parameter extents, where n is the number of continuous and two level (yes-no) nominal input parameters. This design increases the number of required runs exponentially with the number of parameters, and therefore is not a good choice for the eight input parameters considered under analysis. Fractional factorial designs analyze a subset of full factorial runs and are denoted by 2_R^{n-p} designs where n is the number of parameters, p is the equivalent number of parameters that are eliminated by reducing the number of runs, and R is the resolution. The resolution gives an indication of the order of aliased parameter interactions, where different parameter effects are indistinguishable and therefore modeled together as one parameter. Since a 2_R^{n-p} design only tests high and low parameter values, at best a linear model can be constructed.

The number of runs determines the DOFs in the resulting model. One degree of freedom (DOF) is used to estimate the amount of error in the model, another is typically used to estimate the intercept (constant term) of the model. The DOFs not used to estimate the error or intercept are used to find the contributions of individual (first-order) or combined (second-order) input parameters, the terms in Eqn. (3.2).

While analyzing Xpatch[®] ISAR images, where each run can last a few hours or days, it is important to minimize the number of runs while still keeping parameter aliasing to an acceptable level. A 2_V^{8-4} fractional factorial design is used that required

16 runs for 8 (continuous or two level nominal) input parameters. The resolution of V means this design allows no aliasing, or inseparable combination, of first-order effects with second-order effects. First-order effects in a resolution V design are aliased with third-order and higher effects. Therefore, the 2_V^{8-4} model is written as

$$\text{smear} = f(p_1, p_2, p_3, p_4, p_5, p_6, p_7, p_8) \quad (3.3)$$

$$\begin{aligned} &= c_0 + c_1 p_1 + c_2 p_2 + c_3 p_3 + c_4 p_4 + c_5 p_5 + c_6 p_6 + c_7 p_7 + c_8 p_8 \\ &\quad + c_{12} p_1 p_2 + c_{13} p_1 p_3 + c_{23} p_2 p_3 + \dots \end{aligned} \quad (3.4)$$

where p_1 is normalized ray density, p_2 is normalized bandwidth, etc. The first-order aliasing structure for this design is

$$\begin{aligned} p_1 \Rightarrow & p_1 + p_3 p_4 p_6 + p_2 p_3 p_7 + p_2 p_4 p_8 + p_2 p_5 p_6 \\ & + p_4 p_5 p_7 + p_3 p_5 p_8 + p_6 p_7 p_8 + \text{higher - order terms.} \end{aligned} \quad (3.5)$$

$$\begin{aligned} p_2 \Rightarrow & p_2 + p_3 p_4 p_5 + p_1 p_3 p_7 + p_1 p_4 p_8 + p_1 p_5 p_6 \\ & + p_4 p_6 p_7 + p_3 p_6 p_8 + p_5 p_7 p_8 + \text{higher - order terms.} \end{aligned} \quad (3.6)$$

$$\begin{aligned} p_3 \Rightarrow & p_3 + p_2 p_4 p_5 + p_1 p_4 p_6 + p_1 p_2 p_7 + p_1 p_5 p_8 \\ & + p_2 p_6 p_8 + p_4 p_7 p_8 + p_5 p_6 p_7 + \text{higher - order terms.} \end{aligned} \quad (3.7)$$

$$\begin{aligned} p_4 \Rightarrow & p_4 + p_2 p_3 p_5 + p_1 p_3 p_6 + p_1 p_2 p_8 + p_1 p_5 p_7 \\ & + p_2 p_6 p_7 + p_3 p_7 p_8 + p_5 p_6 p_8 + \text{higher - order terms.} \end{aligned} \quad (3.8)$$

$$\begin{aligned} p_5 \Rightarrow & p_5 + p_2 p_3 p_4 + p_1 p_2 p_6 + p_1 p_4 p_7 + p_1 p_3 p_8 \\ & + p_3 p_6 p_7 + p_4 p_6 p_8 + p_2 p_7 p_8 + \text{higher - order terms.} \end{aligned} \quad (3.9)$$

$$\begin{aligned} p_6 \Rightarrow & p_6 + p_1 p_3 p_4 + p_1 p_2 p_5 + p_2 p_4 p_7 + p_2 p_3 p_8 \\ & + p_3 p_5 p_7 + p_4 p_5 p_8 + p_1 p_7 p_8 + \text{higher - order terms.} \end{aligned} \quad (3.10)$$

$$\begin{aligned}
p_7 \Rightarrow p_7 + p_1 p_2 p_3 + p_1 p_4 p_5 + p_2 p_4 p_6 + p_3 p_4 p_8 \\
+ p_3 p_5 p_6 + p_2 p_5 p_8 + p_1 p_6 p_8 + \text{higher - order terms.}
\end{aligned} \tag{3.11}$$

$$\begin{aligned}
p_8 \Rightarrow p_8 + p_1 p_2 p_4 + p_1 p_3 p_5 + p_2 p_3 p_6 + p_3 p_4 p_7 \\
+ p_4 p_5 p_6 + p_2 p_5 p_7 + p_1 p_6 p_7 + \text{higher - order terms.}
\end{aligned} \tag{3.12}$$

The 2_{V}^{8-4} design and its 16 runs allows 14 contributions to be estimated. These contributions are a combination of first and second-order parameter effects. Unfortunately, not all first and second-order contributions can be estimated. Since each scattering geometry is considered separately, a different model is constructed for each model. The estimated contributions are therefore different for each scattering geometry; the contributions are changed as part of the analysis to best fit the experimental cross range smear data gathered for each model.

The 16 runs only test parameter values at the outer extents of the ranges of each continuous parameter with combinations of the two level nominal parameters. Therefore the model derived from these tests is at best linear. By adding runs that test values at the center point of the continuous parameters and for each combination of two level nominal parameters, the analysis can account for response curvature between the parameter extents. Since there are (2) two level nominal parameters, four additional runs are used that test the midpoints of each continuous parameter. With these additional center point runs, the total of runs is increased to 20 and the model can account for quadratic terms. The smear model is then written as

$$\text{smear} = f(p_1, p_2, p_3, p_4, p_5, p_6, p_7, p_8) \tag{3.13}$$

$$\begin{aligned}
= c_0 + c_1 p_1 + c_2 p_2 + c_3 p_3 + c_4 p_4 + c_5 p_5 + c_6 p_6 + c_7 p_7 + c_8 p_8 \\
+ c_{11} p_1^2 + c_{12} p_1 p_2 + c_{13} p_1 p_3 + c_{14} p_1 p_4 \\
+ c_{22} p_2^2 + c_{23} p_2 p_3 + c_{24} p_2 p_4 + \dots
\end{aligned} \tag{3.14}$$

The aliasing structure is unaffected by added center point runs.

The JMP statistical software package, by SAS Institute Inc., is used to generate the required runs and perform the subsequent analysis for the 2_V^{8-4} fractional factorial experiment. Using the parameter ranges defined in Sec. 3.3.1, JMP generates the runs shown in Tab. 3.4.

Once the runs are defined by JMP, Xpatch[®] is used to generate ISAR images (stored as binary .trace files) for each geometry and set of runs. The pixel data is extracted from the ISAR images using the `si2rgb.x` utility. The resulting .iq file (the pixel magnitude of the ISAR image) is then read into Matlab[®] and analyzed for cross range smear where each cross range slice is analyzed for cross range smear per Sec. 2.5. The maximum smear for each image is the smear value used for the subsequent DOE analysis and input parameter characterization.

The same statistical program, JMP, is then used to construct a mathematical model of the SBR and ISAR imaging process. Given all second-order parameters are not included in the model due to DOF limitations, the included second-order parameters are varied to produce a model of least squares best fit. The fit of each model is described by its R^2 value, where an R^2 approaching unity indicates a perfect fit with empirical data, i.e., the calculated parameter coefficients accurately characterize cross range smear. More formally, R^2 is the proportion of the experimental system described by the DOE-calculated model, defined as the sum of squared due to regression (SSR) divided by the total sum of squares (SST) [9]. The R^2 measure is written as

$$R^2 = \frac{\sum_{n=1}^N (\text{smear}_{\text{model},n} - c_0)^2}{\sum_{u=1}^N (\text{smear}_{\text{actual},n} - c_0)^2}. \quad (3.15)$$

where N is the number of runs accomplished and c_0 is the constant parameter in Eqn. (3.4).

Table 3.4: A list of the required runs for the 2_V^{8-4} fractional factorial experiment design, generated with JMP. The Pattern column identifies high (+), low (-), and center (0) parameter values.

Run	DOE Pattern	Ray Density (rays/ λ)	Frequency Extent (GHz)	Frequency Center (GHz)	Frequency Increment (GHz)	Angular Span (Degrees)	Angular Increment (Degrees)	First Bounce Algorithm (PO/SBR)	Diffraction Edge File (Yes/No)
1	-----	5	1	10	0.005	5	0.01	PO	No
2	---++++-	5	1	10	0.01	20	0.1	SBR	No
3	--+-+--+	5	1	15	0.005	20	0.1	PO	Yes
4	--+--++	5	1	15	0.01	5	0.01	SBR	Yes
5	-+---++	5	10	10	0.005	20	0.01	SBR	Yes
6	-+---++	5	10	10	0.01	5	0.1	PO	Yes
7	-++--++	5	10	15	0.005	5	0.1	SBR	No
8	-++++---	5	10	15	0.01	20	0.01	PO	No
9	+-----++	20	1	10	0.005	5	0.1	SBR	Yes
10	+---+---+	20	1	10	0.01	20	0.01	PO	Yes
11	+--+-+--	20	1	15	0.005	20	0.01	SBR	No
12	+---+---	20	1	15	0.01	5	0.1	PO	No
13	++---+---	20	10	10	0.005	20	0.1	PO	No
14	++---+---	20	10	10	0.01	5	0.01	SBR	No
15	+++-----	20	10	15	0.005	5	0.01	PO	Yes
16	+++++++	20	10	15	0.01	20	0.1	SBR	Yes
17	0 0 0 0 0 0 --	12.5	5.5	12.5	0.0075	12.5	0.055	PO	No
18	0 0 0 0 0 0 -+	12.5	5.5	12.5	0.0075	12.5	0.055	PO	Yes
19	0 0 0 0 0 0 +-	12.5	5.5	12.5	0.0075	12.5	0.055	SBR	No
20	0 0 0 0 0 0 ++	12.5	5.5	12.5	0.0075	12.5	0.055	SBR	Yes

3.5 Cross Range Smear Reduction

In addition to the input parameter characterization described in Sec. 3.4, an examination of the smear reduction method proposed by Bhalla and Ling [2] is performed. The proposed smear reduction implements a sliding window filter across constant frequency arcs of the spatial frequency annulus. This aspect averaging reduces discontinuities in the spatial frequency data that, according to Bhalla and Ling, are the angular scintillations that cause cross range smear in the resulting ISAR image.

The averaging technique calls for a 3-aspect sliding window applied across each spatial frequency aspect arc. Before the windowing can be applied, however, the spatial frequency data is exported to a text (.field) file using `ss2field.x`. The data is then read into Matlab[®] and windowed. New data is written out as another .field file, where it is reinserted into the Xpatch[®] SBR/ISAR process (illustrated in Fig. 2.4) using the `ss2trace.x` utility to generate the output ISAR image. This command is the same as used to generate the ISAR image from the unfiltered data. Cross range smear is then analyzed as per Sec. 3.4. Cross range smear in these new images is compared to those that have not been processed with this smear reduction technique.

In addition to the proposed 3-aspect sliding window, a 9-aspect sliding window is implemented for comparison. This extended window is implemented in the same manner as the 3-aspect window, and the analysis is performed identically.

IV. Cross Range Smear Characterization Results

4.1 Introduction

This chapter presents the results and analysis of cross range smear characterization in Xpatch[®] Inverse Synthetic Aperture Radar (ISAR) images. These ISAR images are generated from the geometries and input parameters of Chap. III. For each geometry, a predesignated set of input parameter values is used to generate ISAR images. These images are then individually analyzed for cross range smear. These smear values serve as the basis for the empirical smear model for that geometry. Due to the high dependence of geometry on electromagnetic (EM) scattering, each geometry has its own empirical smear model and is individually discussed.

For each geometry, an empirical cross range smear model is presented and discussed. This model, generated with Design of Experiments (DOE) techniques, approximates the smear computed in an Xpatch[®] ISAR image given a set of parameter inputs. Each model's parameter coefficients characterize how those parameters affect cross range smear given that scattering geometry.

A separate cross range smear model is necessary for each geometry since EM scattering, and therefore ISAR images, are highly dependent on shape. The parameters included in each model are varied to best fit the empirical model to the experimental smear data. The parameters and their coefficients form the smear model as

$$\text{smear} = f(p_1, p_2, p_3, p_4, p_5, p_6, p_7, p_8) \quad (4.1)$$

$$\begin{aligned} &= c_0 + c_1p_1 + c_2p_2 + c_3p_3 + c_4p_4 + c_5p_5 + c_6p_6 + c_7p_7 + c_8p_8 \\ &\quad + c_{11}p_1^2 + c_{12}p_1p_2 + c_{13}p_1p_3 + c_{14}p_1p_4 \\ &\quad + c_{22}p_2^2 + c_{23}p_2p_3 + c_{24}p_2p_4 + \dots \end{aligned} \quad (4.2)$$

where the actual included first and second-order parameters and coefficients vary with each geometries' model. It is important to note that parameters are linearly mapped to vary between -1 and 1 , *so parameter coefficients are directly comparable*. The constant c_0 is referred to as the intercept, and is included in each DOE model for functional completeness.

All first-order parameters are included in each model to serve as a basis for comparison, but additional parameters are changed to enhance R^2 fit and illustrate effect.

4.2 Flat Rectangular Plate

The flat rectangular plate produces ISAR images with smear values given in Tab. 4.1. Using this data, an empirical model with the parameters and parameter coefficients shown in Tab. 4.2 is generated. The model is very well fit due as indicated by its high R^2 value.

The amount of smear varies between between 1500 and 3000. The intercept is by far the largest term, and parameter coefficients are small in comparison. However, parameter coefficients are still distinguishable and meaningfully contribute to the smear model. The largest parameter contribution, by far, is frequency center. Bandwidth is just over 20% less important, followed by the squared ray density term.

The ray density squared contribution is the third strongest, meaning the model has significant curvature over its ray density dimension. The second-order ray density parameter, when combined with angular increment, frequency increment, and angular span, are also of note, although less so than the ray density squared term. The first-order ray density term is almost insignificant. Besides the ray density squared term, therefore, ray density does not contribute a large amount to the smear model. This ray density unimportance is attributable to the perfectly flat geometry, where ray discretization effects are reduced.

Table 4.1: The smear value for each flat rectangular plate ISAR image is given with its constituent input parameters. Each ISAR image is generated using Xpatch[®] with the flat rectangular plate geometry, described in Sec. 3.2.1. The Pattern column identifies high (+), low (-), and center (0) parameter values.

Run	DOE Pattern	Ray Density (rays/ λ)	Frequency Extent (GHz)	Frequency Center (GHz)	Frequency Increment (GHz)	Angular Span (Degrees)	Angular Increment (Degrees)	First Bounce Algorithm (PO/SBR)	Diffraction Edge File (Yes/No)	Smear
1	-----	5	1	10	0.005	5	0.01	PO	No	1903.02
2	---++++-	5	1	10	0.01	20	0.1	SBR	No	1619.73
3	--+++-++	5	1	15	0.005	20	0.1	PO	Yes	2671.94
4	-++--++	5	1	15	0.01	5	0.01	SBR	Yes	2312.11
5	-+---++	5	10	10	0.005	20	0.01	SBR	Yes	2591.64
6	-+---++	5	10	10	0.01	5	0.1	PO	Yes	2145.23
7	-+---++	5	10	15	0.005	5	0.1	SBR	No	3553.98
8	-++++--	5	10	15	0.01	20	0.01	PO	No	3830.17
9	+-----	20	1	10	0.005	5	0.1	SBR	Yes	1736.79
10	+---+---	20	1	10	0.01	20	0.01	PO	Yes	1551.13
11	+---+---	20	1	15	0.005	20	0.01	SBR	No	2960.91
12	+---+---	20	1	15	0.01	5	0.1	PO	No	2672.02
13	++---+--	20	10	10	0.005	20	0.1	PO	No	2671.73
14	++---+--	20	10	10	0.01	5	0.01	SBR	No	2163.46
15	+++-----	20	10	15	0.005	5	0.01	PO	Yes	3197.39
16	+++++++	20	10	15	0.01	20	0.1	SBR	Yes	4393.26
17	000000--	12.5	5.5	12.5	0.0075	12.5	0.055	PO	No	2894.72
18	000000+-	12.5	5.5	12.5	0.0075	12.5	0.055	PO	Yes	2913.16
19	000000+-	12.5	5.5	12.5	0.0075	12.5	0.055	SBR	No	2956.15
20	000000++	12.5	5.5	12.5	0.0075	12.5	0.055	SBR	Yes	2906.84

Table 4.2: Flat Rectangular Plate Smear Model

Parameter	Coefficient
Intercept	2917.72
Frequency Center	575.57
Bandwidth	444.95
Ray Density*Ray Density	-294.31
Angular Span	162.91
Ray Density*Angular Increment	140.44
Ray Density*Frequency Increment	64.15
Ray Density*Angular Span	63.01
Frequency Increment*Angular Increment	61.99
Angular Increment	59.68
Ray Density	44.93
Diffraction Edge File	-40.32
Frequency Increment	-37.52
First Bounce Algorithm	37.22
R^2	0.9670

For the flat rectangular plate, the first bounce algorithm, diffraction edge file, and frequency increment are all relatively insignificant. However, since they are both first-order parameters, they are included as a comparison against other parameter effects.

While the flat rectangular plate may not be the most interesting target, it serves as an excellent comparison with the ridged plate of Sec. 4.3.

4.3 Ridged Plate

The ridged plate produces ISAR images with smear values given in Tab. 4.3. Using this data, an empirical model with the parameters and parameter coefficients shown in Tab. 4.4 is generated. The model is very well fit, evidenced by its high R^2 value.

The amount of smear varies significantly between runs; the standard deviation over all the smear values is just over 1400. This variation indicates the presence of strong parameter coefficients, agreeing with the large numbers seen in Tab. 4.4.

Table 4.3: The smear value for each ridged plate ISAR image is given with its constituent input parameters. Each ISAR image is generated using Xpatch[®] with the ridged plate geometry, described in Sec. 3.2.2. The Pattern column identifies high (+), low (-), and center (0) parameter values.

Run	DOE Pattern	Ray Density (rays/ λ)	Frequency Extent (GHz)	Frequency Center (GHz)	Frequency Increment (GHz)	Angular Span (Degrees)	Angular Increment (Degrees)	First Bounce Algorithm (PO/SBR)	Diffraction Edge File (Yes/No)	Smear
1	-----	5	1	10	0.005	5	0.01	PO	No	435.56
2	----++++-	5	1	10	0.01	20	0.1	SBR	No	419.96
3	---+----+	5	1	15	0.005	20	0.1	PO	Yes	294.64
4	---+----+	5	1	15	0.01	5	0.01	SBR	Yes	293.59
5	-+----++	5	10	10	0.005	20	0.01	SBR	Yes	2885.33
6	-+----++	5	10	10	0.01	5	0.1	PO	Yes	408.07
7	-+----++	5	10	15	0.005	5	0.1	SBR	No	641.98
8	-++++---	5	10	15	0.01	20	0.01	PO	No	4501.35
9	+----+++	20	1	10	0.005	5	0.1	SBR	Yes	380.54
10	+----+++	20	1	10	0.01	20	0.01	PO	Yes	393.46
11	+----+++	20	1	15	0.005	20	0.01	SBR	No	274.16
12	+----+++	20	1	15	0.01	5	0.1	PO	No	248.76
13	++----++	20	10	10	0.005	20	0.1	PO	No	3108.54
14	++----++	20	10	10	0.01	5	0.01	SBR	No	378.75
15	++----++	20	10	15	0.005	5	0.01	PO	Yes	630.39
16	+++++++	20	10	15	0.01	20	0.1	SBR	Yes	4748.81
17	000000--	12.5	5.5	12.5	0.0075	12.5	0.055	PO	No	1046.86
18	000000+-	12.5	5.5	12.5	0.0075	12.5	0.055	PO	Yes	1066.90
19	000000+-	12.5	5.5	12.5	0.0075	12.5	0.055	SBR	No	1059.84
20	000000++	12.5	5.5	12.5	0.0075	12.5	0.055	SBR	Yes	1080.58

Table 4.4: Ridged Plate Smear Model

Parameter	Coefficient
Intercept	1063.55
Bandwidth	910.16
Angular Span	825.54
Ray Density*Angular Increment	822.57
Ray Density*Diffraction Edge File	266.26
Frequency Center	201.47
Ray Density*Ray Density	189.20
Ray Density*First Bounce Algorithm	174.99
Frequency Increment	171.35
Angular Increment	28.67
Ray Density	17.68
Diffraction Edge File	3.33
First Bounce Algorithm	1.45
R^2	0.9989

Similar to the flat rectangular plate of Sec. 4.2, the dominant model term is the intercept. The strongest parameter contribution is bandwidth, followed by angular span and then ray density*angular increment. Other parameters are also significant, but contribute considerably less than these first three parameters.

Of note, ray density does not significantly factor into the model as a first-order effect but does have a very large contribution when combined as a second-order parameter with diffraction edge file, first bounce algorithm, and especially angular increment. The ray density squared term is also significant, contributing curvature to the model across that dimension. Ray density therefore does not have a large linear contribution to the smear for this geometry, but becomes an important factor when considered together with angular increment.

As a group, the frequency dependant terms (bandwidth, frequency center, and frequency increment) are also important to presence of smear. Bandwidth, in this case, is by far the largest contributor of this group. Compared to the flat rectangular plate parameter coefficients, frequency center is much less important in this model;

frequency center has the largest parameter coefficient in the flat rectangular plate smear model but is relegated to fifth largest here.

The use of a diffraction edge file or change in the first bounce algorithm has very little effect on the presence of smear.

4.4 *Slicy*

The slicy geometry produces ISAR images with smear values given in Tab. 4.5. Using this data, an empirical model with the parameters and parameter coefficients shown in Tab. 4.6 is generated. The model is very well fit, evidenced by the high R^2 value.

The amount of smear generated using this geometry does not vary much between runs; the standard deviation over all smear values is just below 230. This lack of variation results in low parameter coefficients. Table 4.6 agrees, showing that parameter coefficients are all much smaller than the intercept term.

By far, the dominant model term is the intercept. The strongest parameter contribution is the frequency center, followed by moderately closely by the ray density squared term and bandwidth. The strength of subsequent parameters decreases greatly from there.

As mentioned, the ray density squared term is very strong, contributing a lot of curvature to the model's ray density dimension. However, the lack of ray density's first-order importance means that over the measured span (5 to 20 rays per wavelength) the difference between the model's low and high side ray density response is relatively small. However, the ray density has a larger effect when combined with angular increment and frequency center as a second-order term .

Bandwidth and frequency center both have strong contributions to the extent of cross range smear. This contribution is similar to other models. Below these two parameters falls angular span, also consistent across models.

Table 4.5: The smear value for each slicy ISAR image is given with its constituent input parameters. Each ISAR image is generated using Xpatch[®] with the slicy geometry, described in Sec. 3.2.3. The Pattern column identifies high (+), low (-), and center (0) parameter values.

Run	DOE Pattern	Ray Density (rays/ λ)	Frequency Extent (GHz)	Frequency Center (GHz)	Frequency Increment (GHz)	Angular Span (Degrees)	Angular Increment (Degrees)	First Bounce Algorithm (PO/SBR)	Diffraction Edge File (Yes/No)	Smear
1	-----	5	1	10	0.005	5	0.01	PO	No	481.08
2	---++++-	5	1	10	0.01	20	0.1	SBR	No	489.66
3	--+++-+	5	1	15	0.005	20	0.1	PO	Yes	821.29
4	-++--++	5	1	15	0.01	5	0.01	SBR	Yes	743.10
5	-+---++	5	10	10	0.005	20	0.01	SBR	Yes	766.74
6	-+---++	5	10	10	0.01	5	0.1	PO	Yes	553.24
7	-+---++	5	10	15	0.005	5	0.1	SBR	No	1041.39
8	-++++--	5	10	15	0.01	20	0.01	PO	No	1113.69
9	+-----	20	1	10	0.005	5	0.1	SBR	Yes	512.72
10	+---+---	20	1	10	0.01	20	0.01	PO	Yes	470.47
11	+---+---	20	1	15	0.005	20	0.01	SBR	No	696.93
12	+---+---	20	1	15	0.01	5	0.1	PO	No	812.63
13	++---+---	20	10	10	0.005	20	0.1	PO	No	822.94
14	++---+---	20	10	10	0.01	5	0.01	SBR	No	534.72
15	+++-----	20	10	15	0.005	5	0.01	PO	Yes	990.57
16	+++++++	20	10	15	0.01	20	0.1	SBR	Yes	1286.60
17	000000--	12.5	5.5	12.5	0.0075	12.5	0.055	PO	No	914.87
18	000000+-	12.5	5.5	12.5	0.0075	12.5	0.055	PO	Yes	873.20
19	000000+-	12.5	5.5	12.5	0.0075	12.5	0.055	SBR	No	899.67
20	000000++	12.5	5.5	12.5	0.0075	12.5	0.055	SBR	Yes	883.85

Table 4.6: Slicy Smear Model

Parameter	Coefficient
Intercept	892.90
Frequency Center	179.66
Ray Density*Ray Density	-134.29
Bandwidth	130.13
Ray Density*Angular Increment	52.36
Angular Span	49.93
Bandwidth*Frequency Center	39.66
Angular Increment	33.95
Ray Density*Frequency Increment	18.25
Angular Span*Angular Increment	12.63
Frequency Increment	-8.10
Ray Density	7.34
First Bounce Algorithm*Diffraction Edge File	6.46
Diffraction Edge File	4.71
Ray Density*Frequency Center	1.07
First Bounce Algorithm	0.07
R^2	0.9968

The first-order effects of a diffraction edge file or first bounce algorithm change is next to negligible. This (lack of) effect is consistent with the results from other geometries' cross range smear models.

4.5 Conclusions

Certain factors, such as target geometry and a few input parameters, influence cross range smear a great deal. Most factors, however, have a varying effect on smear. The choice of Xpatch[®]'s first bounce algorithm or diffraction edge file has almost no effect on cross range smear.

The primary conclusion regarding cross range smear is that, as expected, cross range smear is primarily a function of geometry. This conclusion is supported by the large difference in smear values between geometries. In addition, since ISAR images

vary depending on the scattering geometry¹, comparing the amount of cross range smear in images from one geometry to a dramatically different one is of limited value. However, the variation of input parameters while keeping the geometry constant creates, through DOE analysis, smear characteristics comparable across geometries.

Ray density, as a first-order effect, is consistently a minor influence on cross range smear regardless of geometry. However, when considered as a second-order term with parameters such as angular increment, it has a much larger effect. In addition, there is consistently model curvature induced by a strong ray density squared term. These effects become more influential as the target complexity increases beyond the flat rectangular plate. This result is consistent with Bhalla and Ling's [2] explanation of cross range smear cause as angular scintillation.

The bandwidth and frequency center terms are also important to the creation of cross range smear. In Xpatch[®], ray tubes are bounced from each aspect and the scattered field as a function of frequency is known in closed-form once the ray bounces are complete. There should therefore not be any loss of coherency or unexpected discontinuity over frequency at a constant aspect. However, a general increase in frequency (which both bandwidth and frequency center determine) will increase the scattering target's electrical size, meaning that an effective scattered field representation requires a finer target surface sampling. This requirement may induce unexpected but otherwise minimized aspect-based discontinuities, and is not specifically addressed in Bhalla and Ling's [2] explanation.

Cross range smear is characterized in terms of input parameters for a limited number of geometries, so expanding this characterization to cover several geometries needs to be done carefully. Besides the natural dependence on geometry, frequency center and bandwidth exert an important influence on cross range smear presence.

¹The variation of ISAR images depending on target geometry makes it a powerful scattering signature.

Ray density is also a very important factor, but only as a combined, second-order parameter.

V. Cross Range Smear Reduction Results

5.1 Introduction

This chapter presents the results and analysis of the smear reduction technique proposed by Bhalla and Ling [2] and described in Sec. 3.5. A smear reduction analysis is presented for each geometry used in smear characterization, and a general discussion applicable to all geometries follows. In addition to the proposed smear reduction technique, a similar technique using a 9-aspect extended sliding window is also analyzed.

The smear reduction technique is applied to each Xpatch[®]-generated scattered field file, and the result used by Xpatch[®] to produce an ISAR image. Each image is evaluated for cross range smear as per Sec. 2.5, and the results compared to the unfiltered ISAR image's cross range smear values. For consistency, each ISAR image is shown with a 50 dB dynamic range.

5.2 Flat Rectangular Plate

The flat rectangular plate displays a fair amount of cross range smear, and the smear reduction technique (as originally proposed) performs well. Both the maximum cross range smear, assigned as the smear for the entire image, and the mean cross range smear are reduced in all ISAR images/runs. Figure 5.1 shows the maximum cross range smear over each run, while Fig. 5.2 shows the corresponding mean values.

Using the original 3-aspect smear reduction technique, maximum smear is reduced in every ISAR image except two. The amount of smear reduction varies, however, and is not a linear function of smear value. The 9-aspect smear reduction reduced smear even further.

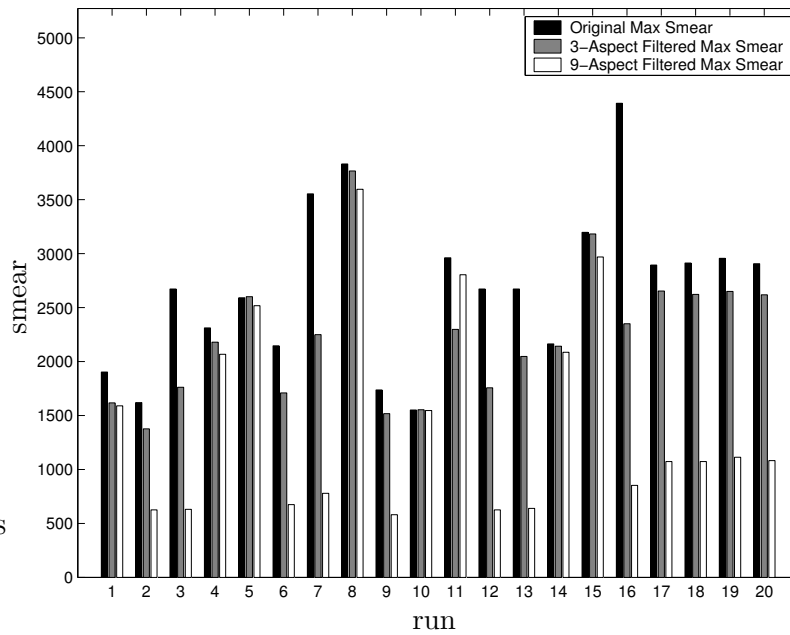


Figure 5.1: A comparison of flat rectangular plate maximum cross range smear reduction by run number. The maximum cross range smear is the smear value assigned to the entire image for the smear characterization.

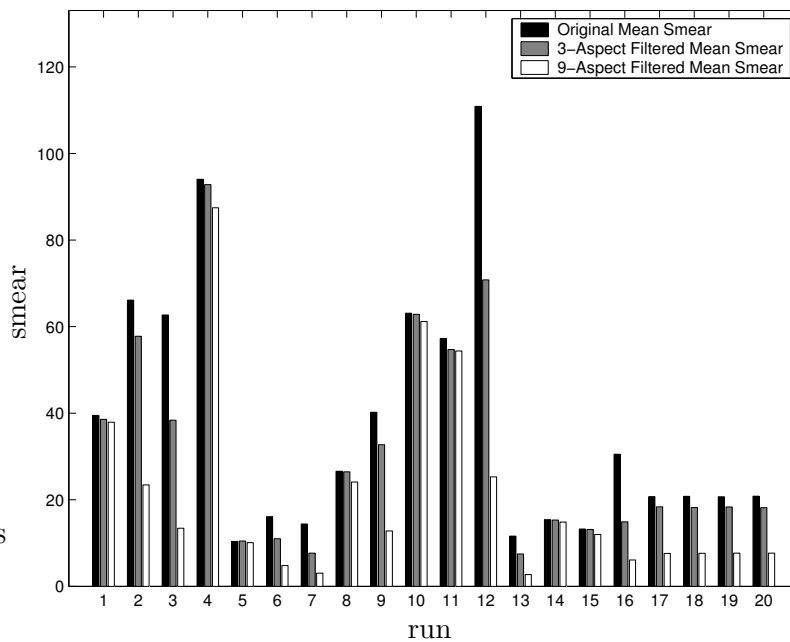


Figure 5.2: A comparison of flat rectangular plate mean cross range smear reduction by run number. The mean cross range smear is computed over each ISAR image's entire range.

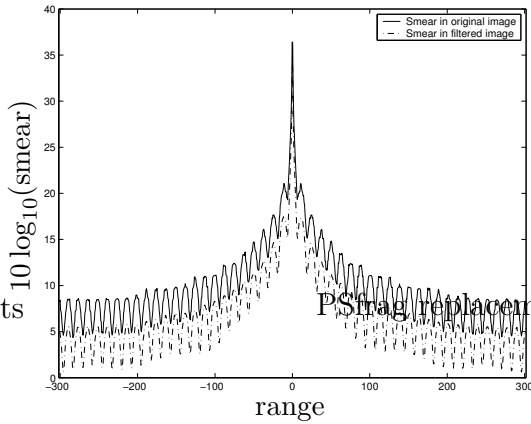


Figure 5.3: Cross range smear in the original and 3-aspect filtered ISAR images for flat rectangular plate run 16. Given this geometry, cross range smear is reduced by the largest amount in this run.

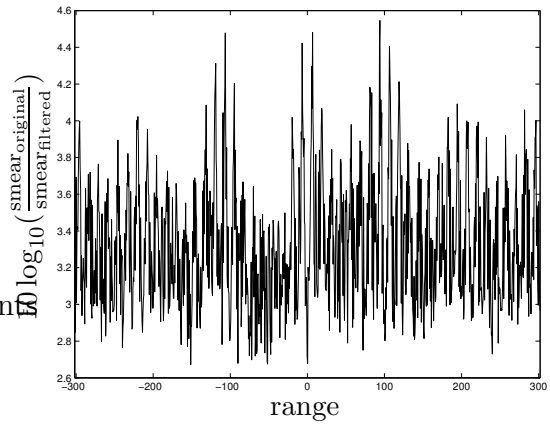


Figure 5.4: The difference in cross range smear between the 3-aspect filtered and original flat rectangular plate run 16 ISAR images. This plot is the difference between the two smear functions in Fig. 5.3.

The smear reduction technique performs best in run 16, which also has the largest (maximum) smear value. The original and 3-aspect filtered ISAR images are shown in Fig. 5.7 and 5.8, respectively. Detailed in Fig. 5.3, smear is almost negligible through all range cells except for where the flat plate scattering return is located. Small smear sidelobes are present due to smeared range-based sidelobes in the ISAR images, but are much weaker than the peak smear value. However, smear reduction is fairly constant across the entire range, through the peak and over the sidelobes. This consistency is illustrated by Fig. 5.4, and visually noticeable in the filtered ISAR image's reduced sidelobes.

The 9-aspect filtered ISAR image is shown in Fig. 5.9. Notably, the smear present above and below the unfiltered plate is reduced below the image's dynamic range. Compared to the original, maximum smear is reduced 81% and mean smear reduced by 80%. The difference in smear is illustrated in Figure 5.5 and 5.6.

The smallest smear reduction, or rather the largest increase, occurs in the image generated with run 5. The original ISAR image is shown in Fig. 5.14. After filtering with a 3-aspect sliding window, the ISAR image shown in Fig. 5.15 is produced.

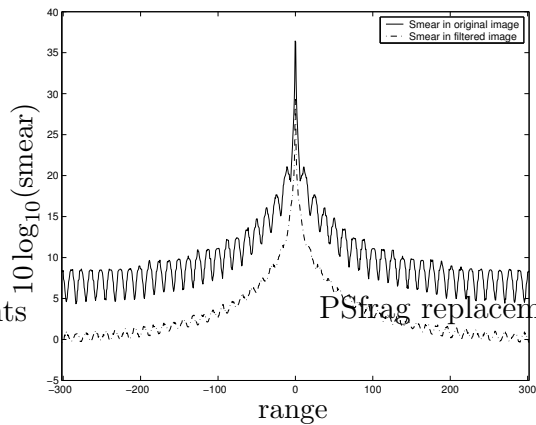


Figure 5.5: Cross range smear in the original and 9-aspect filtered ISAR images for flat rectangular plate run 16. Given this geometry, cross range smear is reduced by the largest amount in this run.

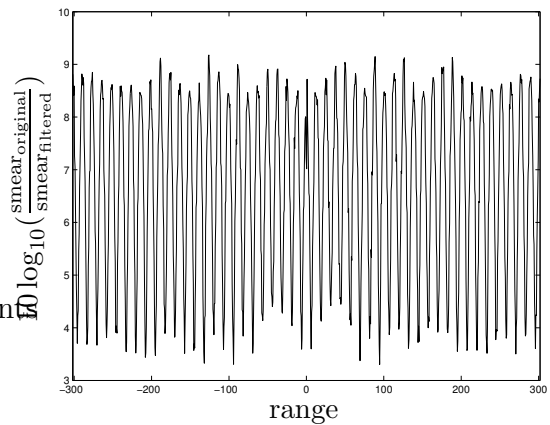


Figure 5.6: The difference in cross range smear between the 9-aspect filtered and original flat rectangular plate run 16 ISAR images. This plot is the difference between the two smear functions in Fig. 5.5.

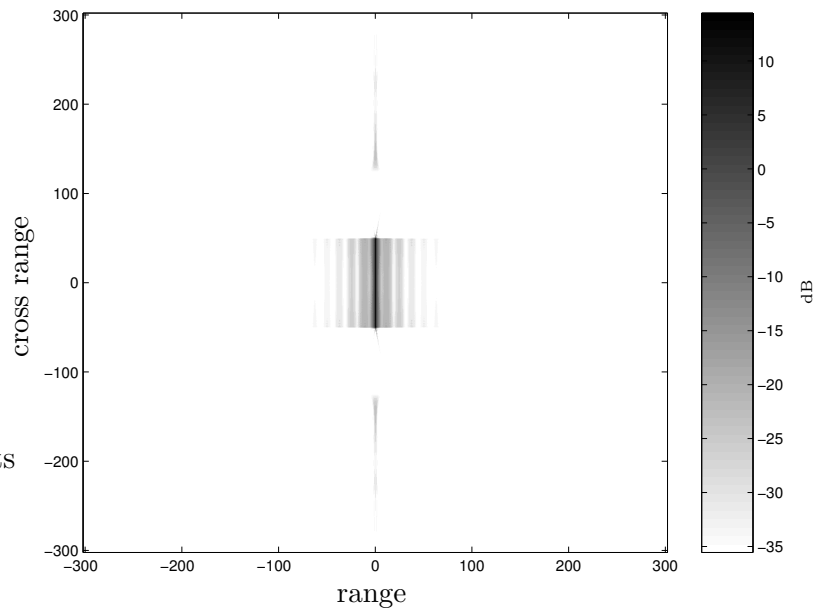


Figure 5.7: The flat rectangular plate ISAR image generated with the parameters given for run 16. This image is unfiltered.

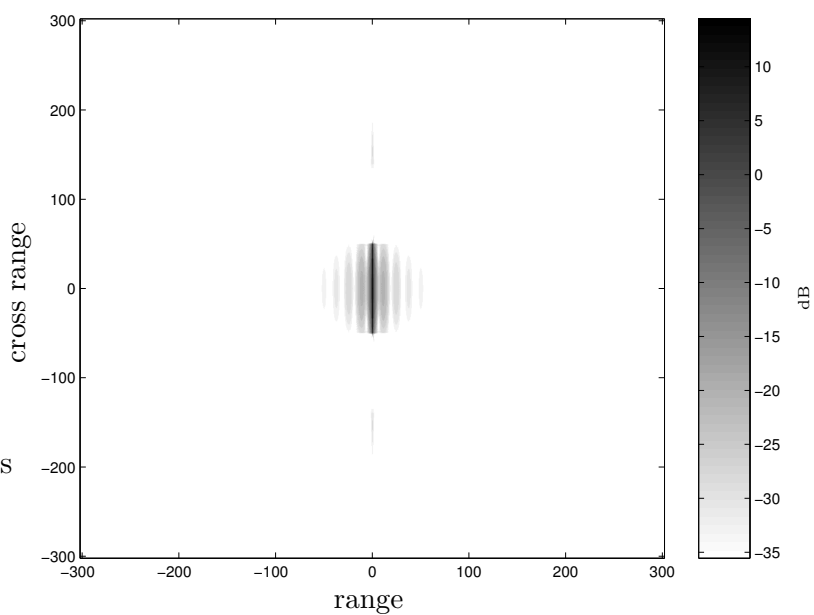


Figure 5.8: The flat rectangular plate ISAR image generated with the parameters given for run 16. This image is filtered with a 3-aspect sliding window, as originally proposed. Maximum cross range smear is reduced by 47%.

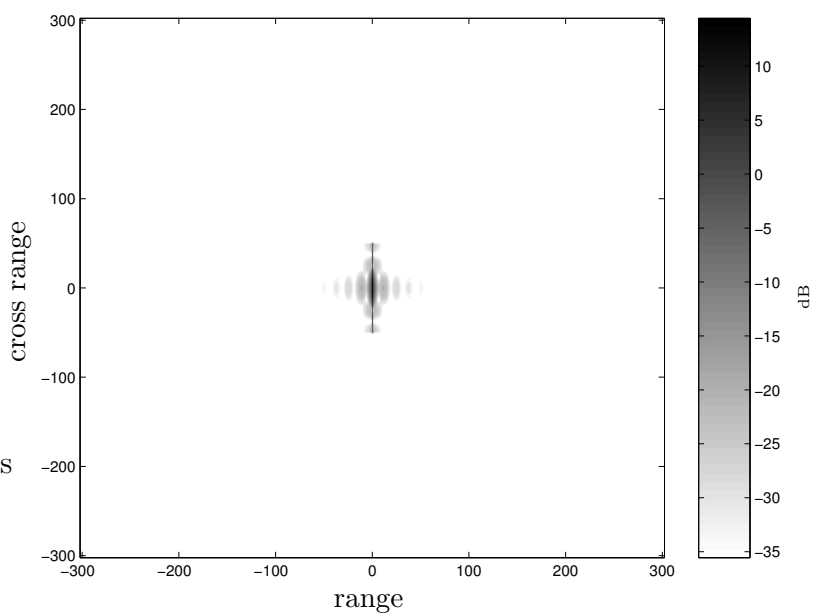


Figure 5.9: The flat rectangular plate ISAR image generated with the parameters given for run 16. This image is filtered with a 9-aspect sliding window, reducing maximum cross range smear by 81%.

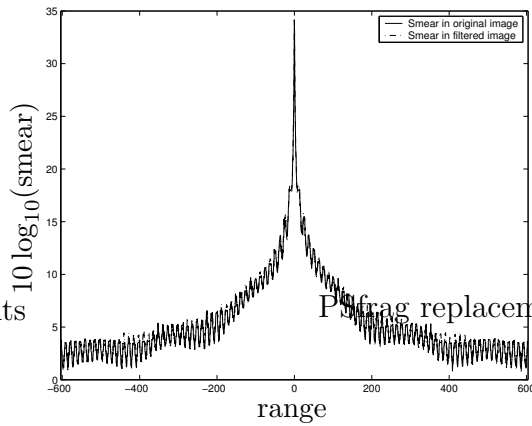


Figure 5.10: Cross range smear in the original and 3-aspect filtered ISAR images for flat rectangular plate run 5. Given this geometry, cross range smear is reduced by the smallest amount in this run. Maximum smear actually increased by a small amount, but mean smear decreased by a similarly small margin.

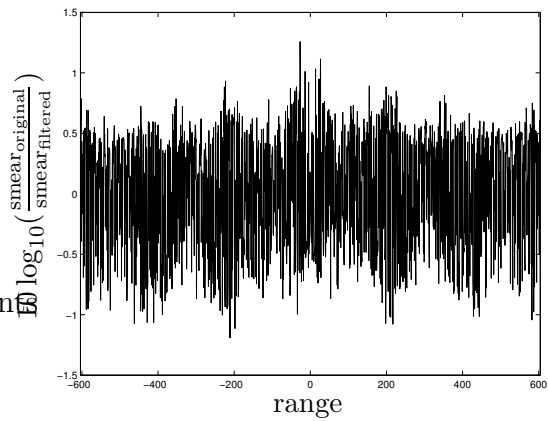


Figure 5.11: The difference in cross range smear between the 3-aspect filtered and original flat rectangular plate run 5 ISAR images. This plot is the difference between the two smear functions in Fig. 5.10.

Given the maximum smear magnitude, approximately 3800, this increase is all but negligible at 0.4%. This small change is reinforced by Fig. 5.10, which shows the amount of change is very small compared to the magnitude of smear. This lack of significant change is seen by the largely overlapping plot. Figure 5.11 shows the net difference between the two smear functions.

When filtered with a 9-aspect sliding window, the ISAR image in Fig. 5.16 is produced. Maximum smear is reduced from the original image by 2%, contrasted with the slight increase using the 3-aspect window. The smear difference between this image and the original is detailed in Fig. 5.12 and 5.13. This lack of significant smear reduction results in nearly identical ISAR images.

5.3 Ridged Plate

The amount of maximum and mean smear present in the ridged plate runs varies significantly, as did the smear reduction technique's performance. In general, smear reduction performs best on runs with large amounts of smear. Also of note, the

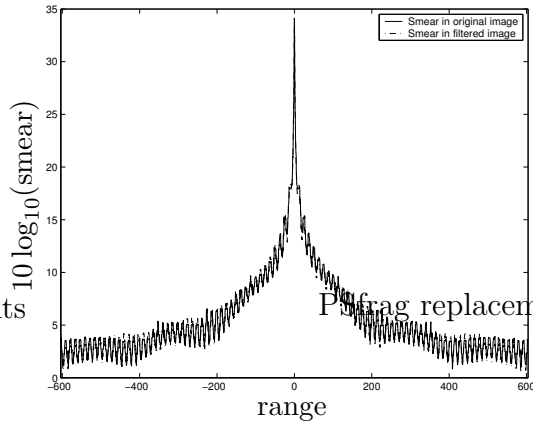


Figure 5.12: Cross range smear in the original and 9-aspect filtered ISAR images for flat rectangular plate run 5. Given this geometry, cross range smear is reduced by the smallest amount in this run. Maximum smear actually increased by a small amount, but mean smear decreased by a similarly small margin.

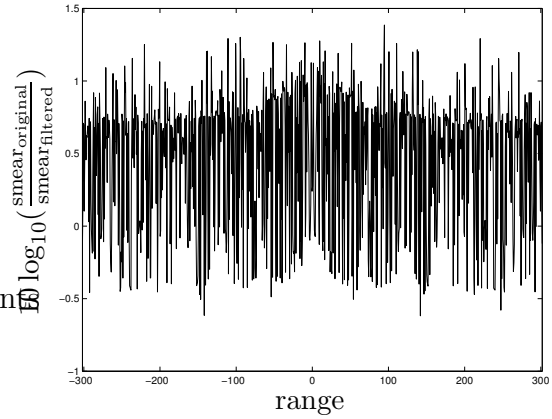


Figure 5.13: The difference in cross range smear between the 9-aspect filtered and original flat rectangular plate run 5 ISAR images. This plot is the difference between the two smear functions in Fig. 5.12.

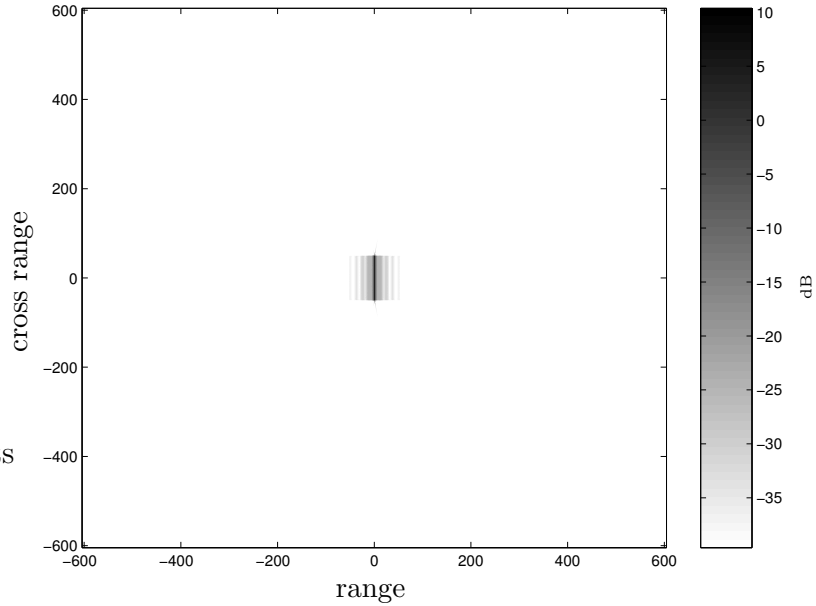


Figure 5.14: The flat rectangular plate ISAR image generated with the parameters given for run 5. This image is unfiltered.

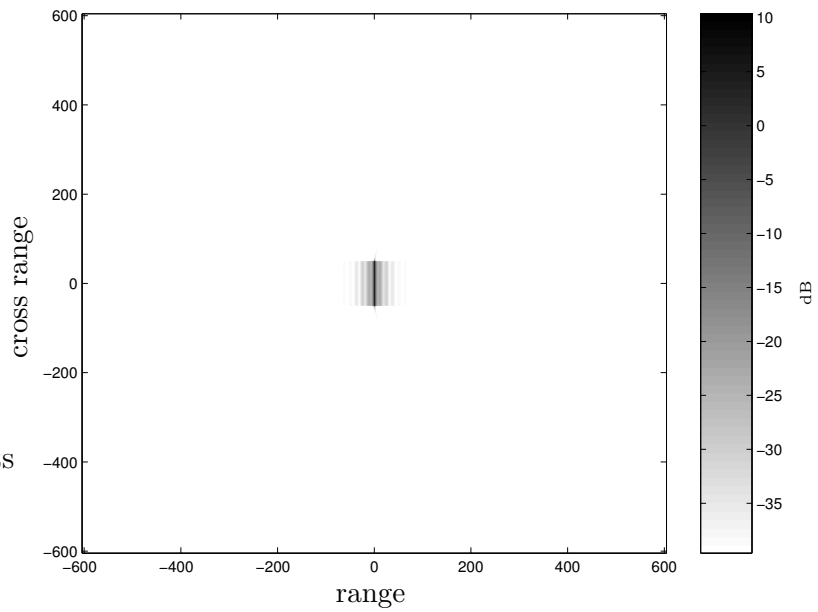


Figure 5.15: The flat rectangular plate ISAR image generated with the parameters given for run 5. This image is filtered with a 3-aspect sliding window, as originally proposed. Maximum cross range smear is increased by approximately 0.4%.

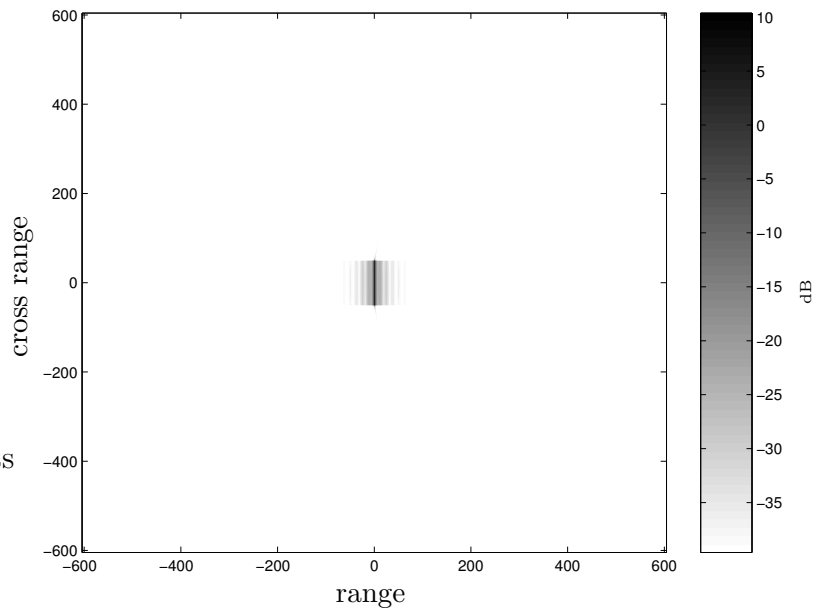


Figure 5.16: The flat rectangular plate ISAR image generated with the parameters given for run 5. This image is filtered with a 9-aspect sliding window, decreasing maximum cross range smear by 3%. However, with this window size, a new low level constant smear is induced. This new smear indicates that the window is too large for this image.

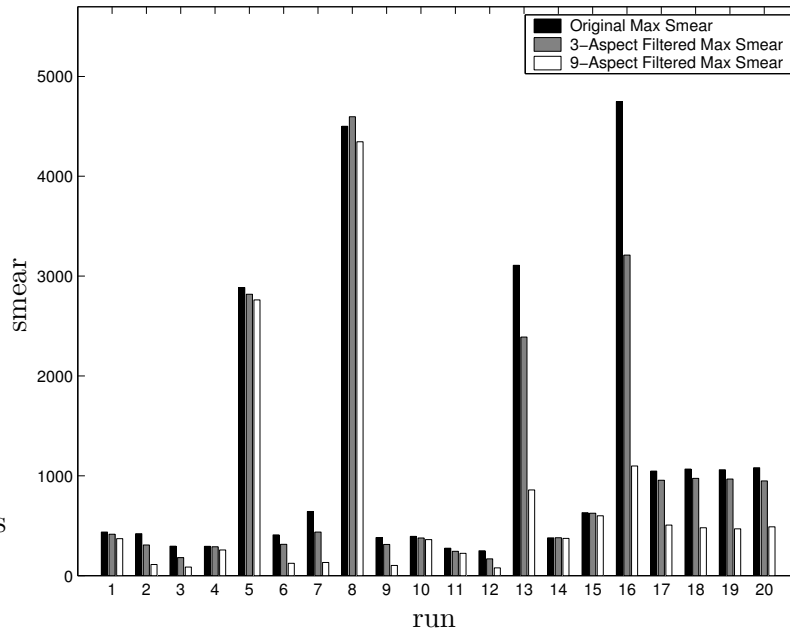


Figure 5.17: A comparison of ridged plate maximum cross range smear reduction by run number. The maximum cross range smear is the smear value assigned to the entire image for the smear characterization.

mean smear values are reduced more consistently than the maximum smear values. This means that the smear reduction technique is more effective at reducing off-peak levels of smear. The amount of smear reduction, in either the maximum or mean case, is not a linear function of smear value. Figure 5.17 shows the maximum cross range smear over each run, while Fig. 5.18 shows the corresponding mean values.

A good example of smear reduction is run 19, where the original image is shown in Fig. 5.23 and the 3-aspect filtered image in Fig. 5.24. The two ISAR images produce smear functions shown in Fig. 5.19. This run does not have the largest maximum or mean smear reduction, but the relatively low maximum value and moderate mean value readily show smear reduction performance. The peak value is present at the ridged plate location, at the downrange center, but a dispersed return further downrange is also smeared. This dispersed response is due to the ridged plate geometry. The smear reduction technique performs well for the smear present on both the maximum and dispersed returns; maximum smear is reduced by 9%.

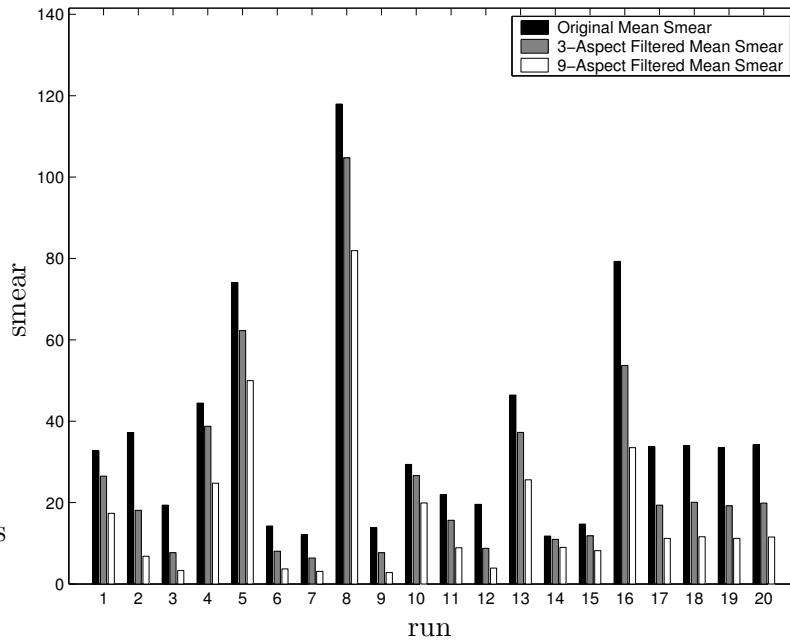


Figure 5.18: A comparison of ridged plate mean cross range smear reduction by run number. The mean cross range smear is computed over each ISAR image's entire range.

The largest reduction, though, is over the dispersed region just downrange of the ridged plate. There, the dispersed scattering response is significantly compressed towards the cross range center. Even though this dispersed region is not the area of maximum smear, as seen in Fig. 5.20 it is the area of largest smear reduction.

The 9-aspect filtered image, shown in Fig. 5.25 has even less smear. A comparison between the original and this filtered ISAR image's smear is given in Fig. 5.21 and 5.22. Here, maximum smear is reduced by just under 55% and mean smear by 67%. The dispersed region is noticeably reduced and compressed towards the middle, even more than the 3-aspect filtered image.

The smallest smear reduction occurs in the image generated with run 8, from the original and 3-aspect filtered ISAR images shown in Fig. 5.30 and 5.31. Maximum and mean smear are both reduced, as shown in Fig. 5.26 and 5.27, but not to the extent seen in other runs. The reduction through the dispersed downrange response is not very evident either, resulting in two nearly identical ISAR images

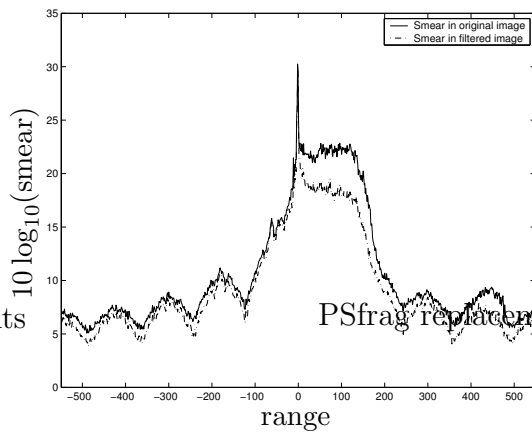


Figure 5.19: Cross range smear in the original and 3-aspect filtered ISAR images for ridged plate run 19. Cross range maximum and mean smear are both successfully reduced between the original and 3-aspect filtered images. This run does not have the largest amount of smear reduction, but overall smear reduction is more readily evident than for other runs due to its relatively low peak value.

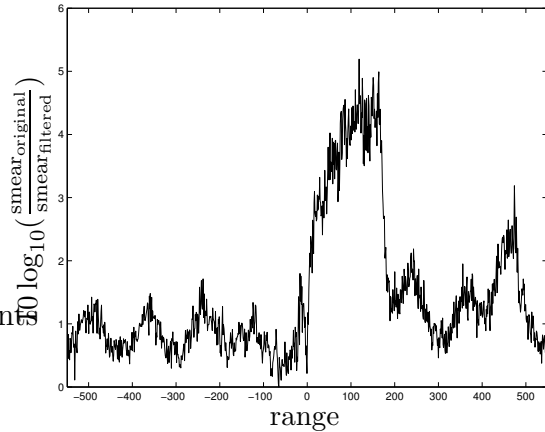


Figure 5.20: The difference in cross range smear between the 3-aspect filtered and original ridged plate run 19 ISAR images. This plot is the difference between the two smear functions in Fig. 5.19.

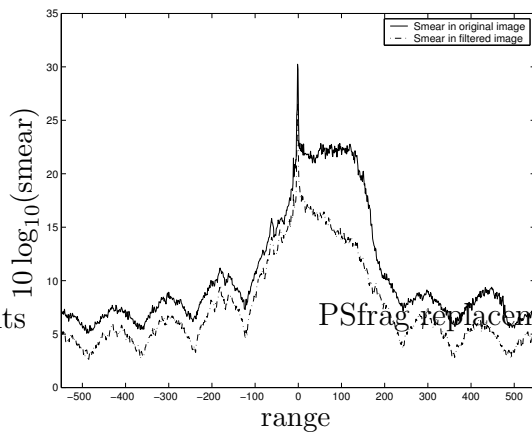


Figure 5.21: Cross range smear in the original and 9-aspect filtered ISAR images for ridged plate run 19. Cross range maximum and mean smear are both successfully reduced. This run does not have the largest amount of smear reduction, but overall smear reduction is more readily evident than for other runs due to its relatively low peak value.

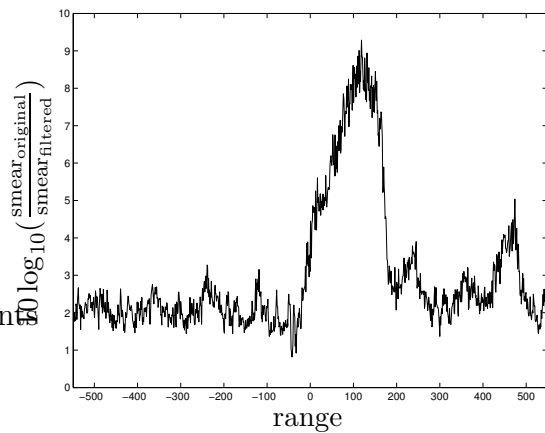


Figure 5.22: The difference in cross range smear between the 9-aspect filtered and original ridged plate run 19 ISAR images. This plot is the difference between the two smear functions in Fig. 5.21.

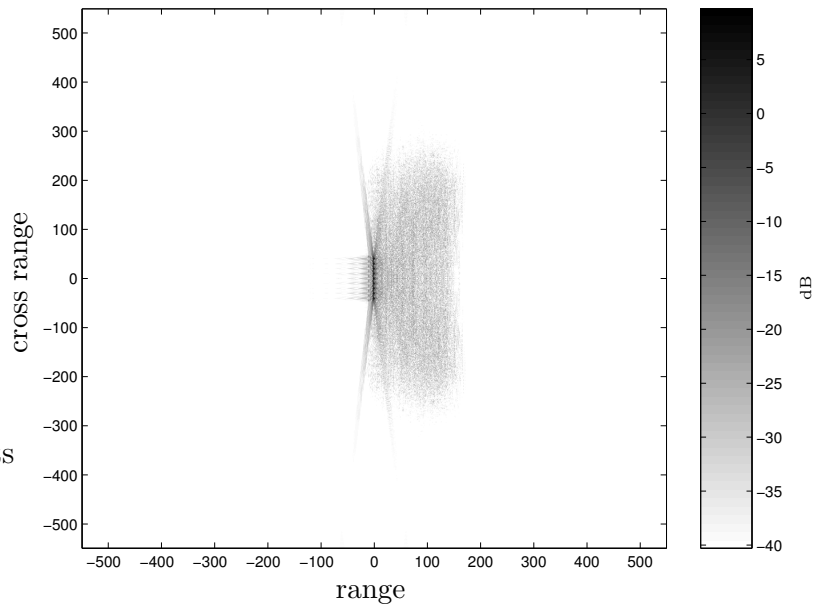


Figure 5.23: The ridged plate ISAR image generated with the parameters given for run 19. This image is unfiltered.

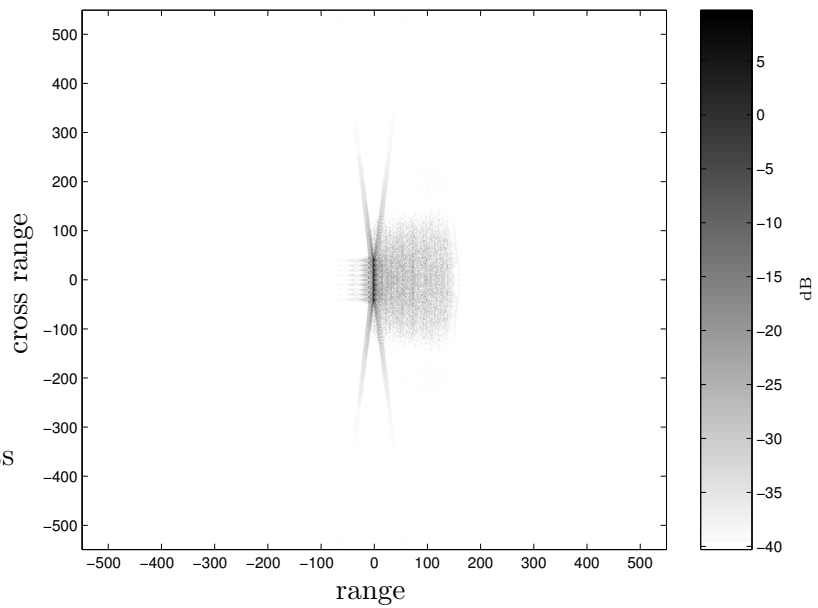


Figure 5.24: The Ridged plate ISAR image generated with the parameters given for run 19. This image is filtered with a 3-aspect sliding window, decreasing maximum cross range smear by approximately 10%.

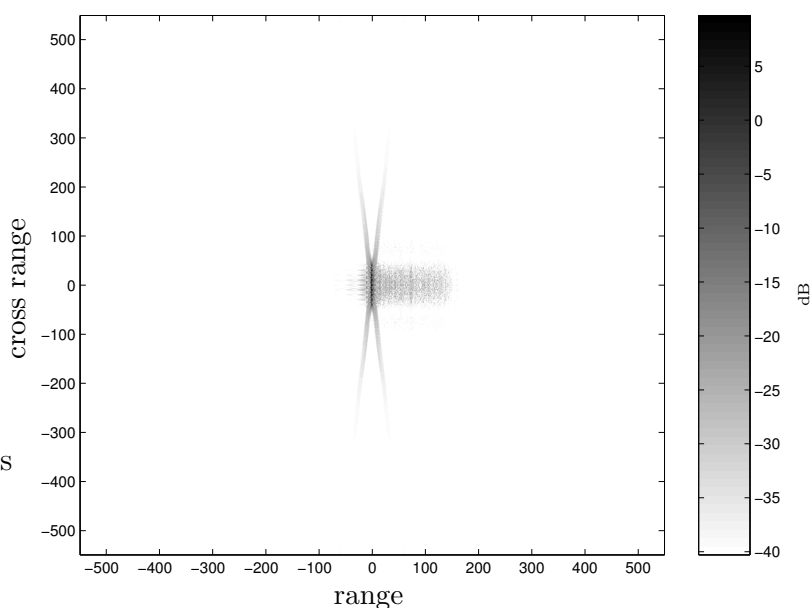


Figure 5.25: The Ridged plate ISAR image generated with the parameters given for run 19. This image is filtered with a 9-aspect sliding window, decreasing maximum cross range smear by approximately 55%.

The 9-aspect filtered image, shown in Fig. 5.32 has less maximum and mean smear than its 3-aspect filtered counterpart. A comparison between the original and this filtered ISAR image's smear is given in Fig. 5.28 and 5.29. Here, maximum smear is reduced by 3% and mean smear by 30% from the original. The dispersed region is noticeably reduced, much more than the original or the the 3-aspect filtered version. This reduction is reflected in the mean smear reduction and is noticeable in the ISAR image as a general reduction and compression towards the center. The 9-aspect filter performs well for this geometry.

5.4 *Slicy*

The amount of maximum and mean smear present in the slicy runs varies a fair amount. The standard deviation of maximum smear over all runs is just over 200 with an mean value of approximately 800. The cross range smear reduction technique's performance as proposed varied by quite a bit, not a linear function of

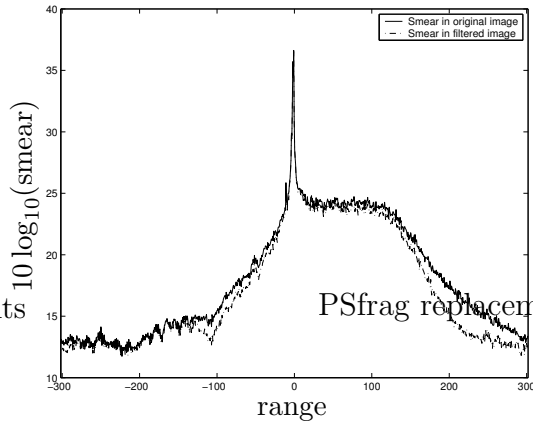


Figure 5.26: Cross range smear in the original and 3-aspect filtered ISAR images for ridged plate run 8. Given this geometry, cross range smear is reduced by the smallest amount in this run. Smear reduction is still evident, especially through the range cells just after the peak.

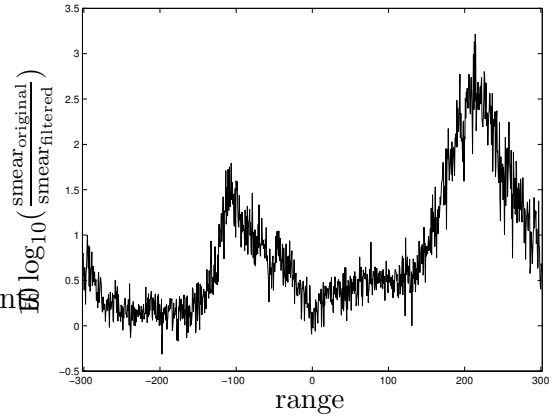


Figure 5.27: The difference in cross range smear between the 3-aspect filtered and original ridged plate run 15 ISAR images. This plot is the difference between the two smear functions in Fig. 5.26.

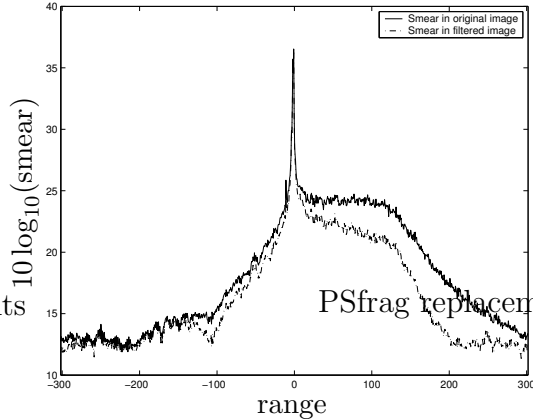


Figure 5.28: Cross range smear in the original and 9-aspect filtered ISAR images for ridged plate run 8. Given this geometry, cross range smear is reduced by the smallest amount in this run. Smear reduction is still evident, especially through the range cells just after the peak.

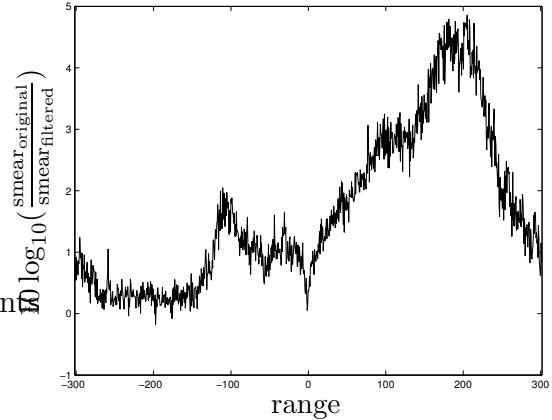


Figure 5.29: The difference in cross range smear between the 9-aspect filtered and original ridged plate run 8 ISAR images. This plot is the difference between the two smear functions in Fig. 5.28.

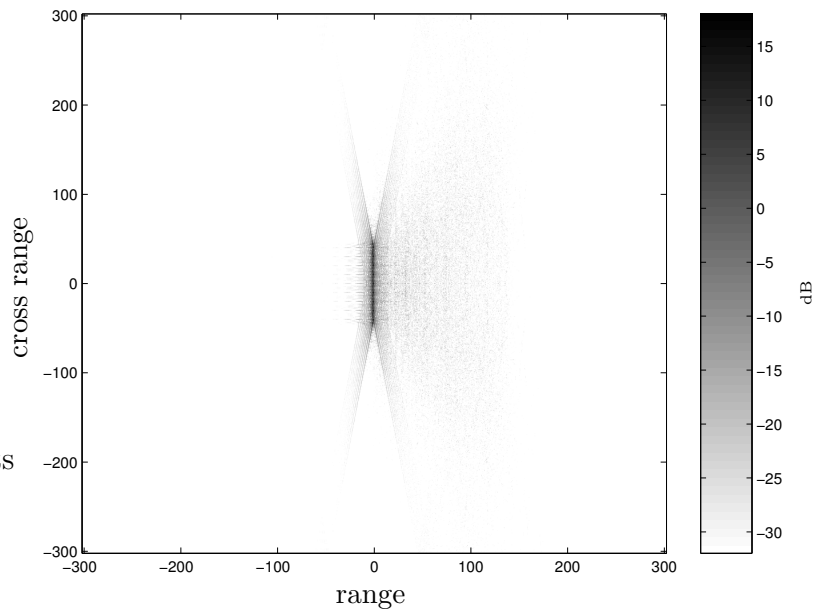


Figure 5.30: The ridged plate ISAR image generated with the parameters given for run 8. This image is unfiltered.

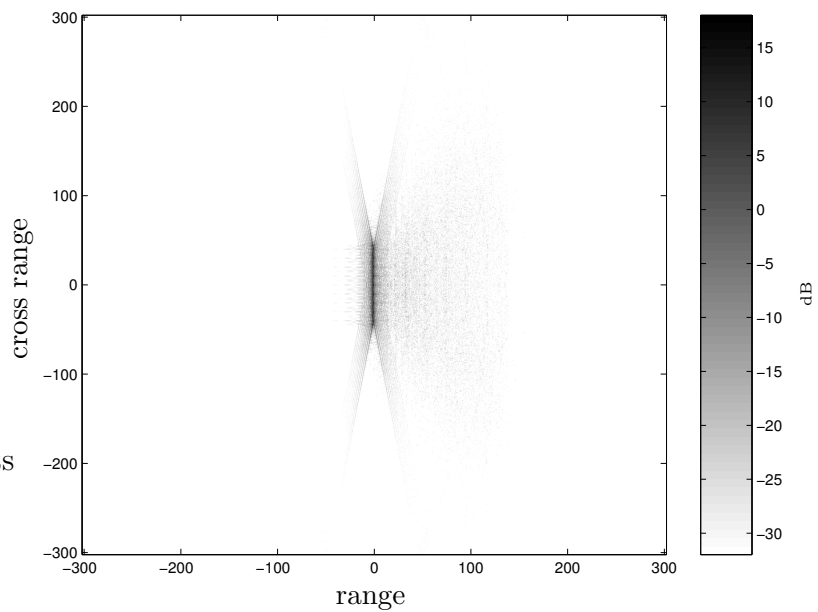


Figure 5.31: The ridged plate ISAR image generated with the parameters given for run 8. This image is filtered with a 3-aspect sliding window, decreasing maximum cross range smear by approximately 2%.

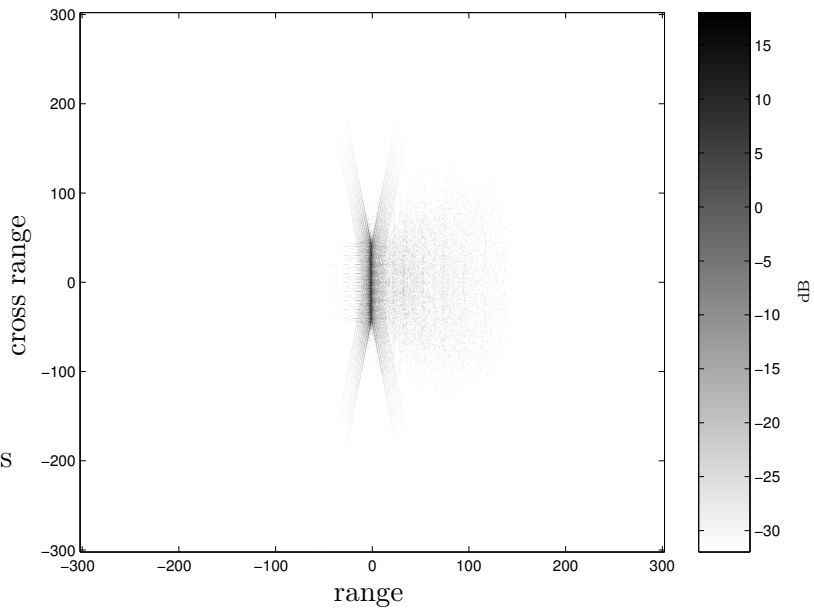


Figure 5.32: The ridged plate ISAR image generated with the parameters given for run 8. This image is filtered with a 9-aspect sliding window, decreasing maximum cross range smear by approximately 3%.

smear value. In all but one case, cross range smear is reduced. Figure 5.33 shows the maximum cross range smear over each run, while Fig. 5.34 shows the corresponding mean values.

A good example of smear reduction is run 12, which produces the original ISAR image shown in Fig. 5.39 and the 3-aspect filtered image in Fig. 5.40. These images produce smear functions shown in Fig. 5.35 and directly compared in Fig. 5.36. The reduction in maximum smear is the second largest at 45%, but run 12 has the largest reduction in mean smear. Smear reduction is noticeable on the cross range smear located at the slicy model's front and middle, as well as over the range-based lobing present throughout the entire image.

The 9-aspect filtered image, shown in Fig. 5.41 has noticeably less maximum smear than its 3-aspect filtered counterpart. A comparison between the original and this filtered ISAR image's smear is given in Fig. 5.37 and 5.38. Here, maximum and

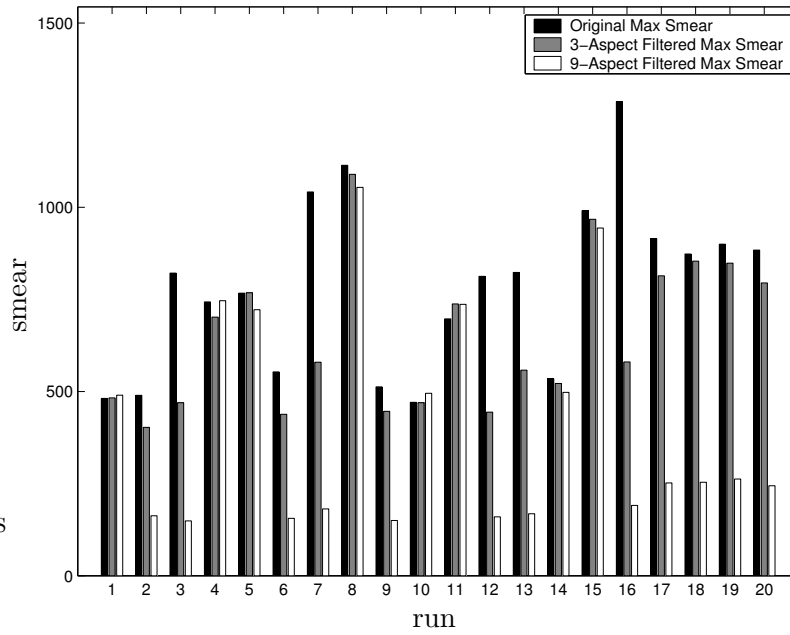


Figure 5.33: A comparison of slicy maximum cross range smear reduction by run number. The maximum cross range smear is the smear value assigned to the entire image for the smear characterization.

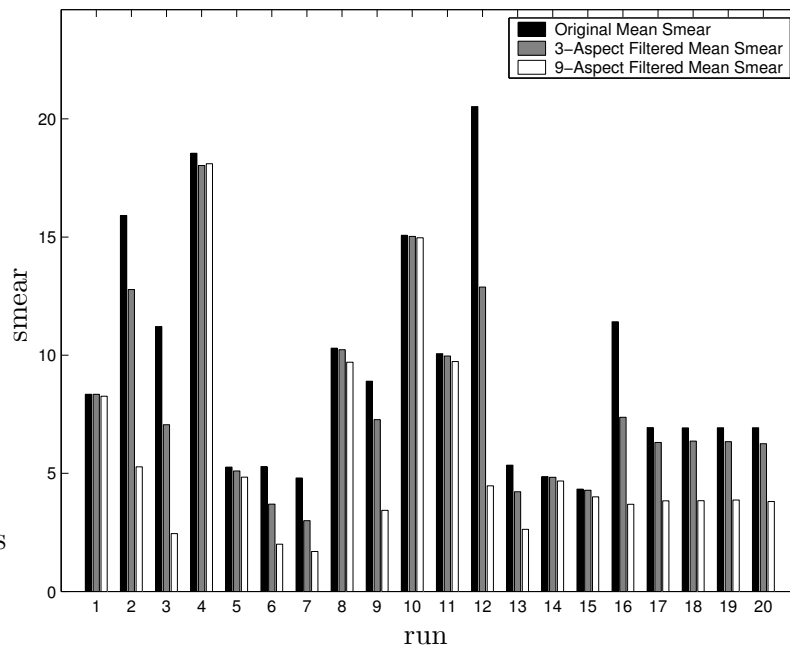


Figure 5.34: A comparison of slicy mean cross range smear reduction by run number. The mean cross range smear is computed over each ISAR image's entire range.

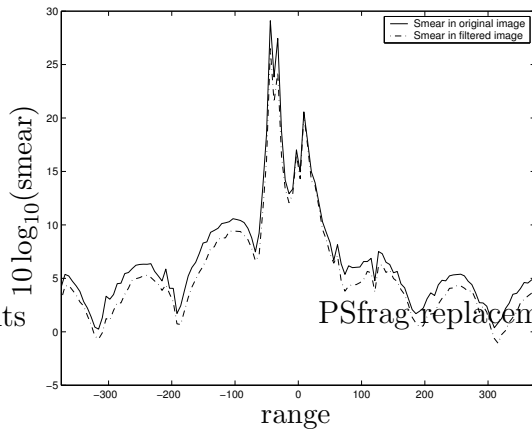


Figure 5.35: Cross range smear in the original and 3-aspect filtered ISAR images for slicy run 12. Cross range maximum and mean smear are both successfully reduced. This run does not have the largest amount of smear reduction, but overall smear reduction is more readily evident than for other runs due to its relatively low peak value.

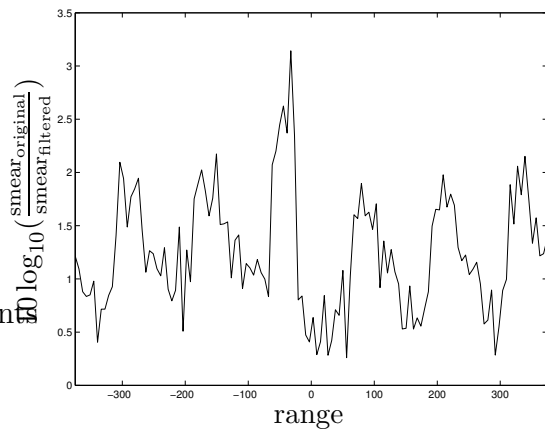


Figure 5.36: The difference in cross range smear between the 3-aspect filtered and original slicy run 12 ISAR images. This plot is the difference between the two smear functions in Fig. 5.35.

smear are reduced by approximately 80%. The 9-aspect filter performs better than the 3-aspect filter in this case.

The smallest smear reduction using the 3-aspect sliding window, actually a small increase in maximum and mean smear, occurs in the image generated with run 1. The smear in the original and filtered ISAR images, Fig. 5.46 and 5.47, is shown in Fig. 5.42. The difference in smear, further detailed in Fig. 5.43, is very small. This small difference makes the two ISAR images appear virtually indistinguishable.

The 9-aspect filtered image, shown in Fig. 5.48 has a little more smear than its 3-aspect filtered counterpart. A comparison between the original and this filtered ISAR image's smear is given in Fig. 5.44 and 5.45. Here, maximum smear is increased by 2% but mean smear is reduced by 1%. The 9-aspect filter performs about the same as the 3-aspect filter in this case.

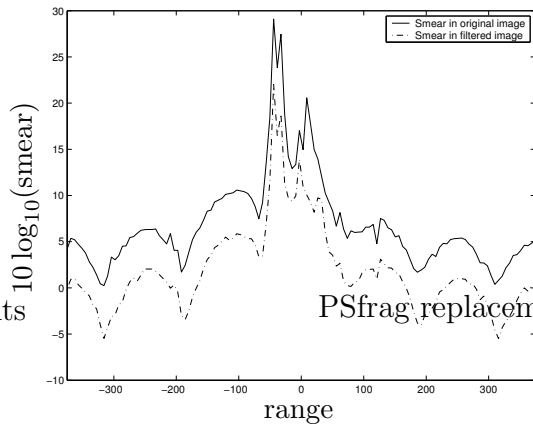


Figure 5.37: Cross range smear in the original and 9-aspect filtered ISAR images for slicy run 12. Cross range maximum and mean smear are both successfully reduced. This run does not have the largest amount of smear reduction, but overall smear reduction is more readily evident than for other runs due to its relatively low peak value.

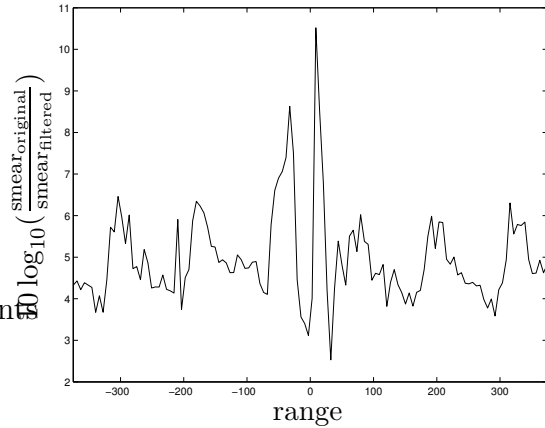


Figure 5.38: The difference in cross range smear between the 9-aspect filtered and original slicy run 12 ISAR images. This plot is the difference between the two smear functions in Fig. 5.37.

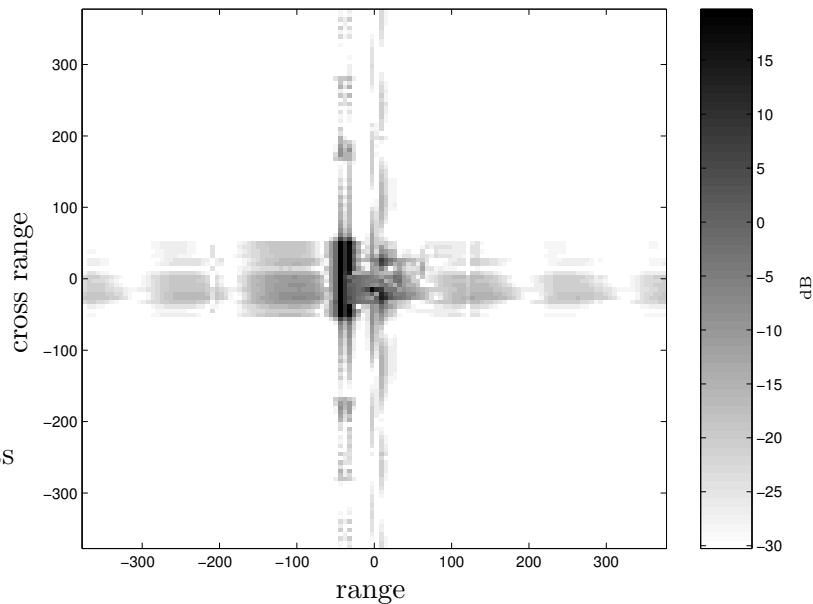


Figure 5.39: The slicy ISAR image generated with the parameters given for run 12. This image is unfiltered.

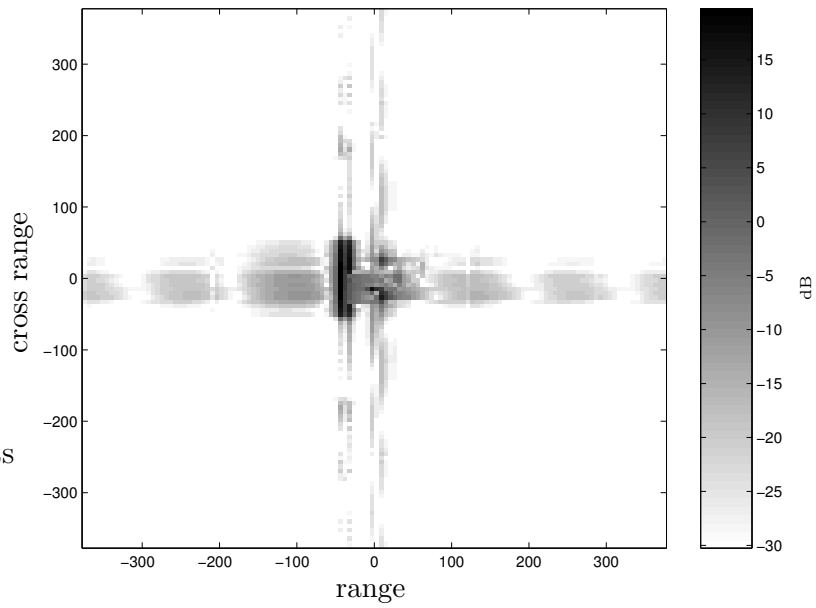


Figure 5.40: The slicy ISAR image generated with the parameters given for run 12. This image is filtered with a 3-aspect sliding window, decreasing maximum cross range smear by approximately 45%.

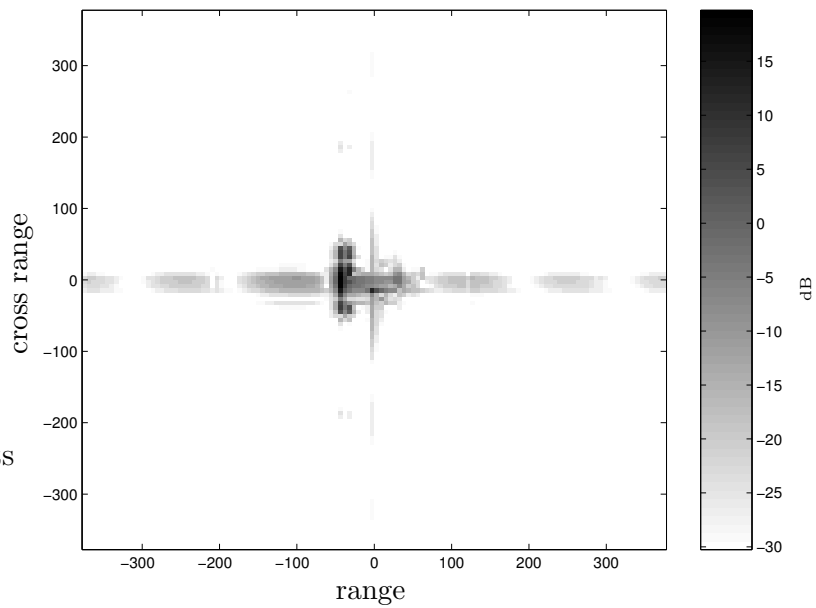


Figure 5.41: The slicy ISAR image generated with the parameters given for run 12. This image is filtered with a 9-aspect sliding window, decreasing maximum cross range smear by approximately 80%.

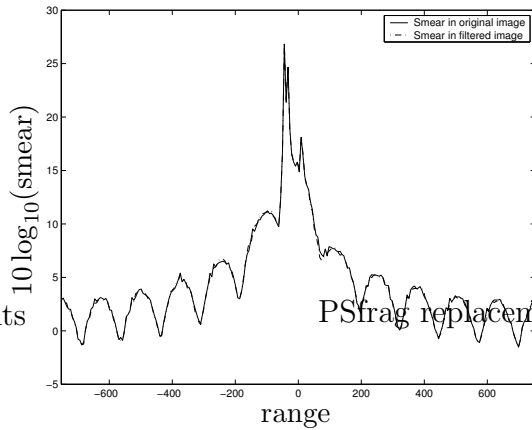


Figure 5.42: Cross range smear in the original and 3-aspect filtered ISAR images for slicy run 1. Given this geometry, cross range smear is just slightly increased, the only run to do so. The amount of change is very small, though, seen by the overlapping plots.

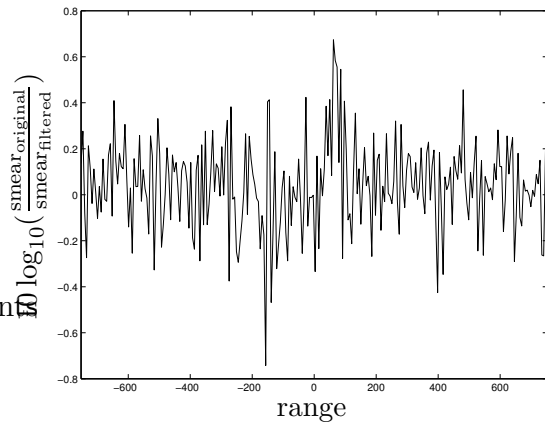


Figure 5.43: The difference in cross range smear between the 3-aspect filtered and original slicy run 1 ISAR images. This plot is the difference between the two smear functions in Fig. 5.42.

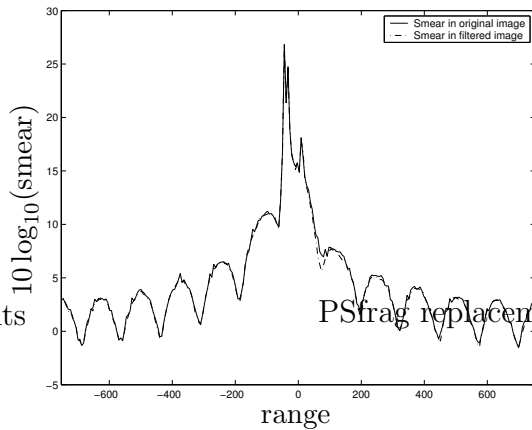


Figure 5.44: Cross range smear in the original and 9-aspect filtered ISAR images for slicy run 1. Given this geometry, cross range smear is just slightly increased, the only run to do so. The amount of change is very small, though, seen by the overlapping plots.

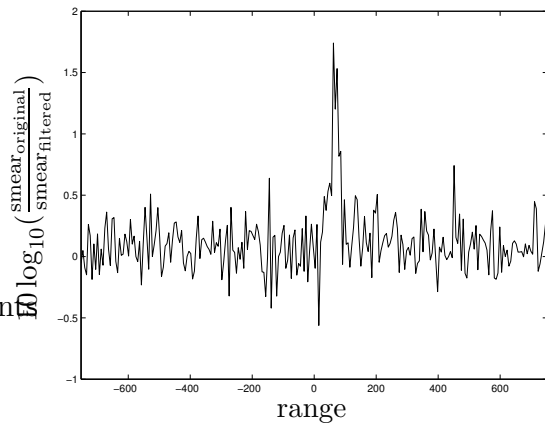


Figure 5.45: The difference in cross range smear between the 9-aspect filtered and original slicy run 1 ISAR images. This plot is the difference between the two smear functions in Fig. 5.44.

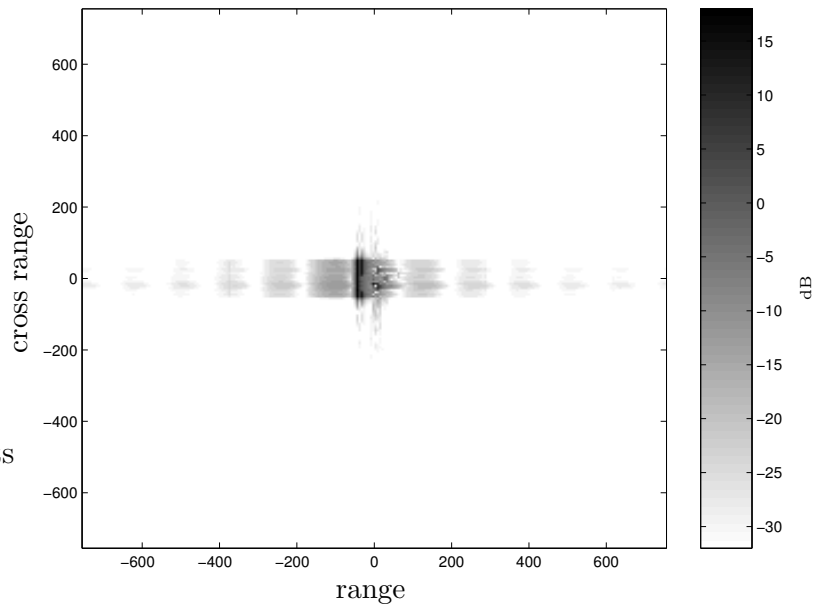


Figure 5.46: The slicy ISAR image generated with the parameters given for run 1. This image is unfiltered.

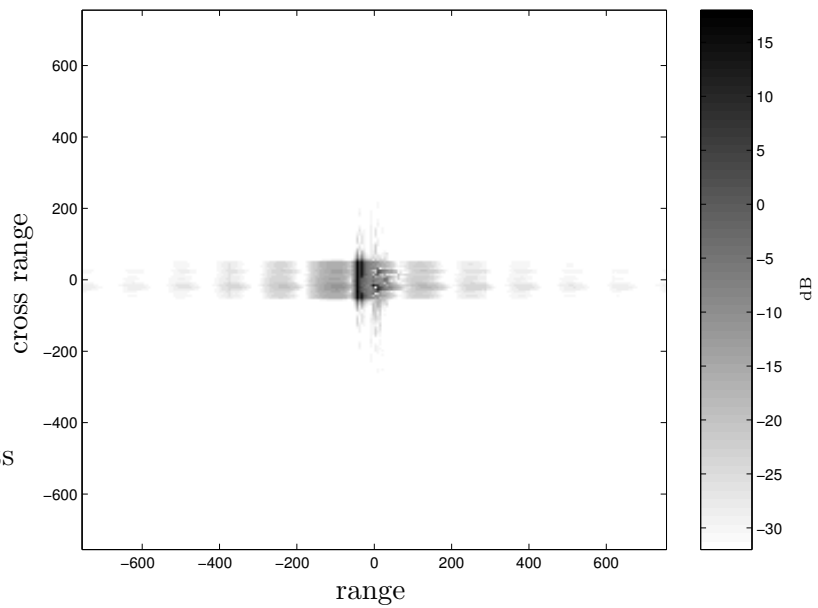


Figure 5.47: The slicy ISAR image generated with the parameters given for run 1. This image is filtered with a 3-aspect sliding window, increasing maximum cross range smear by approximately 0.3%.

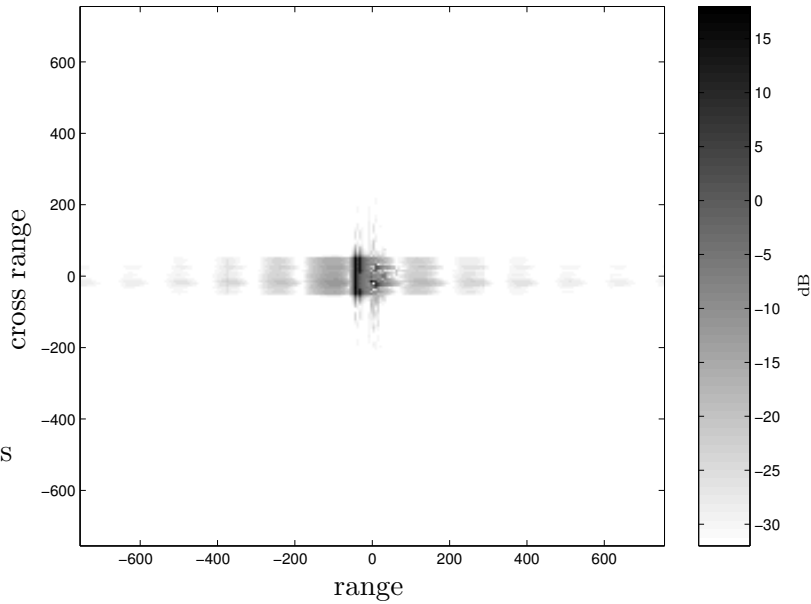


Figure 5.48: The slicy ISAR image generated with the parameters given for run 1. This image is filtered with a 9-aspect sliding window, increasing maximum cross range smear by approximately 2%.

5.5 Conclusions

Overall, the cross range smear reduction technique as proposed by Bhalla and Ling [2] performs well. However, if the sliding window is expanded to 9 aspects, the results are more unpredictable.

Using the originally proposed 3-aspect sliding window, smear is reduced for all but a very few cases, regardless of geometry. In most cases, the amount of smear reduction is significant, both visually and by numerical analysis. However, the amount of smear reduction varies by geometry and, to a lesser extent, other Xpatch[®] parameter values. The smear reduction algorithm also reduces the ISAR image's overall scattering response level.

If the sliding window is expanded to 9 aspects, smear is further reduced in almost all cases. However, this smear reduction also reduces the overall response level. Further increases in window size would further reduce the image brightness.

As can be seen in the ISAR images that show good smear reduction, especially for the ridged plate and slicy geometries, this smear reduction technique can perform very well. In most 3-aspect filtered cases it performs well, with little image degradation. The 9-aspect window usually produces even better results, at a greater reduction in brightness.

Unfortunately, the cross range smear reduction technique's performance is not a linear function of the amount of cross range smear. Cross range smear is reduced by different amounts in every run and geometry combination, making smear reduction prediction very difficult.

VI. Conclusions

6.1 Introduction

This section presents general conclusions about cross range smear in Xpatch[®] Inverse Synthetic Aperture Radar (ISAR) images. Specifically, the two primary facets of this research are discussed: cross range smear characterization and reduction. In addition, future work to characterize and minimize cross range smear is suggested.

6.2 General Discussion

Cross range smear is a non-physical, and therefore erroneous, effect that occurs in Xpatch[®] ISAR images generated with frequency domain computations. The purpose of this work is to facilitate a better understanding of cross range smear, in terms of causes and mitigation. This work characterizes cross range smear in terms of Xpatch[®]'s input parameters and then analyzes a proposed smear reduction technique.

Even though cross range smear is primarily a function of scattering geometry, parameter values have an additional and measurable effect. Through the analysis presented in Chap. IV, the following observations appear consistent through all analyzed geometries.

- Frequency center and bandwidth have a significant first-order effect on cross range smear.
- Ray density does not have a significant first-order, linear effect on cross range smear. Ray density has a quadratic impact over the range of values analyzed in this work. It also has significant second-order influence, especially with the angular increment parameter.

- The choice of Xpatch[®]'s first bounce algorithm or diffraction edge file has negligible effect on cross range smear.
- The scattered field computations took a very long time, even on a 512-processor supercomputer.

As seen in Chap. V, the smear reduction technique proposed by Bhalla and Ling [2] performs well over the geometries analyzed. Using their 3-aspect sliding window, smear is successfully reduced in all but a few cases. Often the smear reduction is significant, with visually apparent improvement. Unfortunately, smear reduction also has the effect of reducing peak response levels throughout the image, slightly reducing overall image contrast.

When the sliding window is increased to 9 aspects, three times that proposed by Bhalla and Ling, cross range smear is generally further reduced. This reduction comes with further peak response level reduction.

6.3 Future Work

This research represents a beginning of a detailed and analytic look into the cross range smear. As such, many opportunities for future work exist. This work concentrates on extending the smear characterization and testing smear reduction implementations.

First, a not-yet-released version of Xpatch[®] implements a cross range smear reduction technique similar to that proposed by Bhalla and Ling [2]. When this version becomes available, a study of smear reduction similar to the work performed and presented in Chap. V is necessary.

Second, more geometries with different scattering characteristics need to be examined. Specifically, cavities and occultating surfaces present very interesting targets with complex scattering properties. These targets have different smearing characteristics for comparison against the targets analyzed in this research.

Bibliography

1. D. Andersh, J. Moore, S. Kosanovich, D. Kapp, R. Bhalla, T. Courtney, A. Nolan, F. German, J. Cook, and J. Hughes, "Xpatch 4: The next generation in high frequency electromagnetic modeling and simulation software," *The Record of the IEEE International Radar Conference*, pp. 844–849, 2000.
2. R. Bhalla and H. Ling, "Cross range streaks in isar images generated via the shooting-and-bouncing ray technique: Cause and solutions," *IEEE Antennas and Propagation Magazine*, vol. 39, pp. 76–80, April 1997.
3. J. Baldauf, S. W. Lee, L. Lin, S. K. Jeng, S. M. Scarborough, and C. L. Yu, "High frequency scattering from trihedral corner reflectors and other benchmark targets: Sbr versus experiment," *IEEE Transactions on Antennas and Propagation*, vol. 39, pp. 1345–1351, Sept 1991.
4. H. Ling, R. Chou, and S. Lee, "Shooting and bouncing rays: Calculating rcs of an arbitrary cavity," in *IEEE Antennas and Propagation Society International Symposium Digest*, vol. 24, June 1986.
5. D. C. Munson and R. L. Visentin, "A signal processing view of strip-mapping synthetic aperture radar," *IEEE Transactions of Acoustics, Speech, and Signal Processing*, vol. 37, pp. 2131–2147, December 1989.
6. C. V. Jakowatz, *Spotlight-Mode Synthetic Aperture Radar: A Signal Processing Approach*. Kluwer Academic Publishers, 1999.
7. W. G. Carrara, R. S. Goodman, and R. M. Majewski, *Spotlight Synthetic Aperture Radar Signal Processing Applications*. Artech House, 1995.
8. J. B. Keller, "A survey of short wavelength diffraction theory," *Electromagnetic Theory and Antennas*, no. 1, pp. 3–9, 1963.
9. A. I. Khuri and J. A. Cornell, *Response Surfaces*, vol. 81. Marcel Dekker, Inc, 1987.

REPORT DOCUMENTATION PAGE

*Form Approved
OMB No. 0704-0188*

The public reporting burden for this collection of information is estimated to average 1 hour per response, including the time for reviewing instructions, searching existing data sources, gathering and maintaining the data needed, and completing and reviewing the collection of information. Send comments regarding this burden estimate or any other aspect of this collection of information, including suggestions for reducing the burden, to Department of Defense, Washington Headquarters Services, Directorate for Information Operations and Reports (0704-0188), 1215 Jefferson Davis Highway, Suite 1204, Arlington, VA 22202-4302. Respondents should be aware that notwithstanding any other provision of law, no person shall be subject to any penalty for failing to comply with a collection of information if it does not display a currently valid OMB control number.

PLEASE DO NOT RETURN YOUR FORM TO THE ABOVE ADDRESS.

1. REPORT DATE (DD-MM-YYYY) 23-03-2004	2. REPORT TYPE Master's Thesis	3. DATES COVERED (From - To) Aug 2003 - Mar 2004
--	--	--

4. TITLE AND SUBTITLE CROSS RANGE SMEAR CHARACTERIZATION IN XPATCH ISAR IMAGES	5a. CONTRACT NUMBER
	5b. GRANT NUMBER
	5c. PROGRAM ELEMENT NUMBER

6. AUTHOR(S) Muend, Peter, E., Capt, USAF	5d. PROJECT NUMBER
	5e. TASK NUMBER
	5f. WORK UNIT NUMBER

7. PERFORMING ORGANIZATION NAME(S) AND ADDRESS(ES) Air Force Institute of Technology Graduate School of Engineering and Management (AFIT/EN) 2950 Hobson Way, Building 640 WPAFB OH 45433-7765	8. PERFORMING ORGANIZATION REPORT NUMBER AFIT/GE/ENG/04-18
---	--

9. SPONSORING/MONITORING AGENCY NAME(S) AND ADDRESS(ES) Dr. Vincent J. Velten Technical Advisor AFRL/SNAS (AFMC) 2241 Avionics Circle WPAFB OH 45433-7321 937-904-9147	10. SPONSOR/MONITOR'S ACRONYM(S)
	11. SPONSOR/MONITOR'S REPORT NUMBER(S)

12. DISTRIBUTION/AVAILABILITY STATEMENT
APPROVED FOR PUBLIC RELEASE; DISTRIBUTION UNLIMITED

13. SUPPLEMENTARY NOTES

14. ABSTRACT
This thesis investigates a cross range smear phenomenon seen in far field, frequency domain Xpatch calculations. The phenomenon is very subtle, manifesting itself in 2-D ISAR images as a low-level scatterer response smeared in the cross range direction. This cross range smear occurs only using complex target models with certain characteristics. It is also a mathematical construct, not occurring in physical SAR systems. Using a carefully constructed scattering target set, Xpatch-generated ISAR images are used to characterize cross range smear in terms of its input parameters. The characterization is done as a DOE-based polynomial approximation to the observed smear levels. Frequency extent and bandwidth have the highest effect on cross range smear, consistently increasing smear with parameter value. Ray density is slightly less important, having primarily squared and second order influence. The choice of diffraction and first bounce algorithm has very little effect on cross range smear. In addition, the performance of a proposed smear reduction technique is analyzed against Xpatch-generated ISAR images. The algorithm generally reduces smear, but the smear reduction magnitude is not a linear function of smear value.

15. SUBJECT TERMS
SYNTHETIC APERTURE RADAR
RADAR IMAGES
ELECTROMAGNETIC WAVE REFLECTIONS
MULTIVARIATE ANALYSIS

16. SECURITY CLASSIFICATION OF:			17. LIMITATION OF ABSTRACT UU	18. NUMBER OF PAGES 107	19a. NAME OF RESPONSIBLE PERSON Todd Hale, Maj, USAF (ENG)
a. REPORT U	b. ABSTRACT U	c. THIS PAGE U			19b. TELEPHONE NUMBER (Include area code) 937-255-2024, email:todd.hale@afit.edu